International Journal of Biological Macromolecules 370 (2026) 152662

Contents lists available at ScienceDirect

International Journal of Biological Macromolecules

journal homepage: www.elsevier.com/locate/ijbiomac

Development of a magnetic xanthan gum-polyacrylamide hydrogel embedding Cu-BTC with antibacterial properties for wound healing applications

Fereshte Hassanzadeh Afruzi [a,*], Majid Abdouss [b], Sohrab Asgaran [c], Zahra Moazzami Goudarzi [d], Rasoul Esmaeely Neisiany [a]

[a] Department of Polymer Engineering, Hakim Sabzevari University, Sabzevar, 9617976487, Iran
[b] Department of Chemistry, Amirkabir University of Technology, Tehran, 1591634311, Iran
[c] Helmaco Sp. Z o.o. Company, Ostrobramska 101/335K, 04-041, Warsaw, Poland
[d] Laboratory of Polymers and Biomaterials, Institute of Fundamental Technological Research, Polish Academy of Sciences, Pawinskiego 5B, Warsaw, 02–106, Poland

ARTICLE INFO

Keywords:
MOF-based hydrogel
Antibacterial
Cu-BTC
Xanthan gum
Wound healing

ABSTRACT

The design of multifunctional hydrogel platforms with strong antibacterial and pro-healing activity is essential for next-generation wound dressings. In this work, a novel nanocomposite hydrogel was fabricated by grafting polyacrylamide onto xanthan gum, crosslinking with borax, incorporating Fe_3O_4 nanoparticles, and inducing in-situ growth of Cu-BTC MOF within the magnetic hydrogel matrix. This integrated structure represents an efficient innovation among MOF–hydrogel systems by combining the biocompatibility of XG, the functional network provided by PAAm, the magnetic features of Fe_3O_4, and the controlled Cu^{2+}-based antibacterial activity of Cu-BTC. Characterization confirmed successful formation and stable polymer–MOF interactions, accompanied by favorable physicochemical properties including superparamagnetic behavior (saturation magnetization ~8 emu/g), relatively high surface area (56.90 m^2/g), and improved thermal stability. The biological assessments were assessed for wound-healing relevance. Swelling of the hydrogels was measured at different pH values (4.0, 5.5, 7.4) and in varying ionic strengths, showing the highest uptake for XG-*grafted*-PAAm, while Fe_3O_4 and Cu-BTC reduced swelling by increasing crosslinking, supporting moisture retention and compact structure in wound environments. Furthermore, the magnetic XG-*grafted*-PAAm @Cu-BTC nanocomposite showed antibacterial activity, with MIC/MBC values of 125/250 μg/mL against *E. coli* and 500/1000 μg/mL against *S. aureus*. Cytocompatibility testing revealed acceptable viability at low–moderate concentrations (91–54% at 1.9–15.6 μg/mL), while the scratch assay confirmed accelerated fibroblast migration at 3.9 μg/mL, indicating a pronounced pro-healing effect. Overall, the synergistic antibacterial action, controlled Cu^{2+} release, hydration capacity, and favorable cell-migration response position this MOF–magnetic hydrogel system as a promising candidate for advanced wound dressings.

1. Introduction

Skin, the largest organ in the human body, is highly susceptible to damage from burns, injuries, or surgeries. When this barrier is compromised due to injury, the wound healing process is initiated to restore tissue integrity [1]. Wound healing is a complex, multi-phase process involving hemostasis, inflammation, proliferation, and remodeling. Bacterial infections pose significant challenges during healing and threaten human health [2]. Microorganisms in the surrounding environment are key contributors to chronic wound infections, as they invade the wound, form colonies, and penetrate deeper tissue layers, ultimately impeding the healing process [3]. Wound dressings play a critical role in preventing infections, maintaining a moist environment, and absorbing wound exudates. An ideal dressing should absorb toxins, retain moisture, enable gaseous exchange, provide insulation, prevent infections, and be non-toxic. Recent advancements demand additional features, such as comfort, durability, non-adherence, easy removal, and the ability to deliver antimicrobial agents and healing mediators without delaying recovery [4].

Hydrogels, with excellent hydrophilicity, biocompatibility, and

* Corresponding author.
E-mail address: Fafruzi@yahoo.com (F.H. Afruzi).

https://doi.org/10.1016/j.ijbiomac.2026.152662
Received 21 August 2025; Received in revised form 28 April 2026; Accepted 21 May 2026
Available online 22 May 2026

three-dimensional structure, have emerged as leading candidates for wound care and have garnered significant research interest, particularly in the past decade. These soft materials maintain a moist environment, absorb excess exudate, provide non-adhesive coverage for delicate tissues, and reduce pain through cooling. Their ECM-like polymeric networks enable active intervention by incorporating antibacterial agents or growth factors, making them effective delivery systems for localized and sustained release of bioactive molecules [5]. Hydrogels derived from natural polysaccharides have been extensively explored for wound management due to their structural similarity to the extracellular matrix, biocompatibility, and biodegradability. These natural-based hydrogels are particularly appealing as wound dressings because they promote hemostasis, reduce inflammation, and support cell proliferation, accelerating the healing process [2]. Xanthan gum (XG), a high molecular weight)range from $1 * 10^6$ to $20 * 10^6$ mol/g(polysaccharide produced by *Xanthomonas campestris*, was FDA-approved in 1969 as a safe, non-toxic polymer, enabling its widespread use as a stabilizer and thickener in food products [6] XG is composed of a β-1,4-D-glucopyranose backbone with a trisaccharide side chain containing mannose (β-1,4), glucuronic acid (β-1,2), and a terminal mannose unit [7]. XG chains are rich in hydroxyl and carboxyl polar groups, contributing to their strong hydrophilic nature. As a result, XG-based hydrogels demonstrate a swelling capacity of up to 26 g/g, making them effective for quickly absorbing wound exudates. Additionally, the XG chains adopt a five-fold helical structure, stabilized by non-covalent interactions between hydroxyl and carboxyl groups, and can undergo conformational changes triggered by temperature or salt [8]. Furthermore, XG-based hydrogels exhibit excellent biocompatibility and biodegradability, making them safe for use in biomedical applications. These hydrogels also support a moist wound environment, promote cell proliferation, and can be functionalized with bioactive agents like antimicrobial nanoparticles or growth factors to enhance wound healing [9]. Although Polysaccharide-based hydrogels are widely used in biomedical applications due to their biocompatibility and biodegradability, they often suffer from inadequate mechanical strength and excessive swelling, which prohibit their efficacy in practical applications. To address these issues, researchers have explored various strategies, such as combining synthetic polymers, forming cross-links, and integrating nanoparticles or nanomaterials. These approaches aim to improve structural integrity and performance in wound healing. For example, in a recent study, reported by Song Tang and co-workers in 2022, Xanthan gum (XG) was combined with polyacrylamide (PAAm) to create hydrogels with enhanced functionality, including 0.36 MPa tensile strength and 2078% stretchability. The hydrogels exhibited excellent water uptake (swelling ratio of 1200%) and demonstrated biocompatibility, adhesion, and self-healing capabilities. Loaded with Cefixime and growth factor, they showed sustained release, inactivated bacteria, and accelerated wound healing in a mouse model [8]. Gutierrez-Reyes et al. developed 3D printable hydrogels by crosslinking gelatin and xanthan gum with glutaraldehyde. The crosslinked hydrogels exhibited varying porosity, swelling, and degradation properties, and demonstrated biocompatibility, supporting the growth of human keratinocytes and fibroblasts. [10] Persistent bacterial infections can delay wound healing by causing prolonged inflammation, hindering the transition to the proliferative stage. Few natural polymers balance both antibacterial properties and biocompatibility. Therefore, combining self-healing abilities and high antibacterial activity is an emerging approach for developing advanced hydrogel dressings for effective wound healing [11].

Nanomaterial reinforcement is a promising method to improve the mechanical and antibacterial functionalities of hydrogels. Nanomaterials like silver, copper, zinc oxide, and titanium dioxide nanoparticles are utilized to create antibacterial-reinforced hydrogels. However, challenges such as cytotoxicity, uncontrolled metal ion release, and limited biodegradability require further optimization in the design of these nanocomposite hydrogels [12]. In this context, MOFs have emerged as a promising option due to their porous and crystalline metal–ligand frameworks, which provide high surface areas, tunable pore sizes, abundant active sites, and enable efficient drug loading and controlled release [13]. They generally exhibit low toxicity and possess intrinsic antibacterial and angiogenic properties, while their features can be tailored through functional group modification, defect engineering, and the choice of metal ions and linkers. However, their instability and partial decomposition in hydrophilic environments limit direct use in aqueous systems. Integrating MOFs into hydrogels improves their dispersion, stability, and overall functionality, enabling composites with controlled release, enhanced antibacterial effects for wound healing [14]. MOF-199 or HKUST-1, also known as Cu-BTC, has garnered attention for its distinctive antibacterial properties and potential in wound healing applications [15]. Research has shown that incorporating MOF-199 into hydrogels significantly influences the wound healing process, enhancing its effectiveness [16]. Nevertheless, direct blending of MOFs with hydrophilic polymer matrices commonly leads to poor dispersion, structural degradation of the MOF in aqueous environments, and inconsistent antibacterial performance. These limitations highlight a critical gap: the need for a robust integration strategy that stabilizes MOFs within hydrogels while enabling controlled release of bioactive ions and maintaining structural integrity.

Magnetic-responsive biocomposites have emerged as powerful smart platforms capable of remotely regulating wound-related biological processes through magneto-mechanical, magneto-thermal, and magneto-electrical stimulation. Among them, magnetic hydrogels represent one of the most promising classes of next-generation wound dressings. Their hydrated, viscoelastic polymeric networks maintain a moist healing environment, protect the wound from external contaminants, and support cell proliferation and migration, while the incorporation of iron oxide nanoparticles imparts external-field responsiveness that enables precise modulation of cellular behavior, controlled drug release, and targeted tissue regeneration. Under magnetic or near-infrared stimulation, these hydrogels can produce localized mechanical cues, mild hyperthermia, or electrical signals, thereby accelerating re-epithelialization, collagen deposition, angiogenesis, and overall tissue remodeling [17].

In the present work, a MOF-hydrogel nanocomposite was synthesized by in-situ growth of Cu-BTC MOF into a crosslinked xanthan gum-based hydrogel matrix. Initially, Fe_3O_4 nanoparticles were prepared via a co-precipitation method. The magnetic xanthan gum-*grafted*-polyacrylamide (XG-*grafted*-PAAm) hydrogel was synthesized via the graft copolymerization of acrylamide onto xanthan gum, followed by crosslinking using borax, a non-toxic crosslinking agent, and then incorporation of pre-prepared Fe_3O_4 into the hydrogel matrix during the polymerization process, resulting in a composite material with enhanced functionality. In the final step, the Cu-BTC MOF was constructed onto the magnetic hydrogel, magnetic XG-*grafted*-PAAm**,** via a facile in-situ growth approach.

Compared to previous MOF-based hydrogel systems, the present work introduces a distinct multi-component design in which Cu-BTC MOF and Fe_3O_4 nanoparticles are synergistically integrated within an eco-friendly XG-*grafted*-PAAm network through in-situ MOF growth. This configuration is intended to exploit the complementary roles of each component: xanthan gum for biocompatibility and hydration, PAAm for functionality, Fe_3O_4 for magnetic responsiveness and catalytic enhancement of ROS production, and Cu-BTC for controlled Cu^{2+} release and intrinsic antibacterial activity, thereby creating a multifunctional platform with improved structural stability, sustained antimicrobial performance, and compatibility with biological environments. These offered synergistic effects were subsequently examined through antibacterial assays (MIC/MBC), cytocompatibility evaluations, and scratch-wound migration tests, collectively supporting the rationale for employing this integrated MOF–magnetic hydrogel framework for wound healing applications.

2. Materials and methods

2.1. Materials

Ethanol, Methanol, and Dimethylformamide (DMF), Ammonium hydroxide 28%, were purchased from Merck. $FeCl_2{\cdot}4H_2O$, $FeCl_3{\cdot}6H_2O$, Cu $(NO_3)_2.3H_2O$, acrylamide, Ammonium persulfate (APS), Sodium tetraborate decahydrate)Borax(, and Benzene-1,3,5-tricarboxylic acid were obtained from Sigma-Aldrich. FT-IR spectra were recorded using a Shimadzu 8400 S (Japan) spectrometer in the range of 4000–400 cm^{-1} with a resolution of 4 cm^{-1} and 32 scans, using the KBr pellet method. The powder sample was mixed with spectroscopic-grade KBr, pressed into pellets, and analyzed at room temperature. Field Emission Scanning Electron Microscopy (FESEM) was employed to analyze the surface morphology of the samples. Three samples (Fe_3O_4 MNPs, Cu-BTC, and the magnetic XG-*grafted*-PAAm@Cu-BTC), were examined using a KYKY-EM8000 (China) operating at an accelerating voltage of 15 kV, while the other two samples (XG, and XG-*grafted*-PAAm were analyzed using a Tescan Vega SEM (Czech Republic) at 20 kV. Prior to imaging, the powdered samples were sputter-coated with a thin layer of gold to enhance conductivity. Micrographs were obtained at various magnifications to evaluate surface features and particle distribution. AFM analysis was performed using a MultiMode AFM (Ara Pazhohesh) in tapping mode with RTESPA-300 probes (k = 40 N/m). The scan was performed over a 10 μm × 10 μm area with a scan rate of approximately 0.8 Hz, and the resolution was set to 512 × 512 pixels 10 × 10 μm scans (0.8 Hz, 512 × 512 pixels) were processed with 2nd order flattening (NanoScope Analysis). X-ray diffraction (XRD) patterns were obtained with a Bruker D8 Advance (USA) diffractometer, using Cu Kα radiation (λ = 0.1542 nm) at 40 kV and 30 mA. The thermal stability of the prepared samples was analyzed by thermogravimetric analysis (TGA) using a BAHR-STA 504 (USA) instrument. Each sample (~10 mg) was heated from room temperature to 800 °C at a heating rate of 10 °C/min under a nitrogen atmosphere with a flow rate of 50 mL/min. The magnetic properties of the samples were measured using a vibrating sample magnetometer (VSM, Meghnatis, Daneshpajooh Kashan Co., Iran). The hysteresis loops were recorded at room temperature in applied fields ranging from −10 kOe to +10 kOe with a sweep rate of 200 Oe/s. The sample mass was approximately 20 mg. The surface area and porosity of the samples were analyzed by N_2 adsorption-desorption at 77 K using a BELSORP Mini II analyzer) BEL Japan, Inc., Japan). Prior to BET measurements, samples were degassed under vacuum at different temperatures based on their thermal stability: Fe_3O_4 nanoparticles at 200 °C for 4 h, while Cu-BTC and other samples at 100 °C for 6 h to prevent structural degradation.

2.2. Methods

2.2.1. Preparation of Fe_3O_4 magnetic nanoparticles (MNPs)

Fe_3O_4 MNPs were synthesized using a co-precipitation method. For this, 0.86 g (4.325 mmol) of $FeCl_2{\cdot}4H_2O$ and 2.35 g (8.694 mmol) of $FeCl_3{\cdot}6H_2O$ were dissolved in 40 mL of distilled water and added to a glass bottle. The bottle was heated at 80 °C for 15 min to ensure complete dissolution of the salts. Subsequently, 10 mL ammonia solution (28%) was added dropwise to the heated solution under a nitrogen atmosphere and continuously stirred until the pH reached 10. During this process, the color of the mixture gradually changed to black, indicating the formation of solid magnetic particles. The reaction was continued for an additional 1 h. The obtained product was cooled to room temperature. The precipitate was then collected using a magnet and washed multiple times with distilled water to remove unreacted salts and excess ammonia. Finally, the obtained nanoparticles were dried in an oven at 80 °C for 12 h.

2.2.2. Preparation of Cu-BTC MOF

MOF-199 was synthesized using a modified version of the procedure reported by Yaghi and colleagues [18].1.36 mmol (0.0.328 g) of Cu $(NO_3)_2.3H_2O$ and 0.84 mmol (0.174 g) of Trimesic acid (benzene-1,3,5-tricarboxylic acid or H_3BTC) were dissolved in a mixture of DMF, ethanol, and distilled water in equal proportions, with a total solvent volume of 9 mL. The solution was stirred for 20 min. The reaction was carried out in a 50 mL Teflon-lined reactor, which was sealed and heated to 80 °C for 24 h. After decanting the hot mother liquor and rinsing with DMF, the product was soaked in methanol, with the solvent replaced three times during this period. The product was activated at 200 °C under atmospheric pressure.

2.2.3. Synthesis of XG-grafted-PAAm copolymer

The graft copolymerization of acrylamide (AAm) onto xanthan gum was conducted via free radical polymerization. A solution of 1 g XG in 50 mL distilled water was stirred at 60 °C for 25 min and degassed by the flow of nitrogen gas for about 20 min. Next, APS solution (1 mmol in 25 mL of water) was gradually added to the above solution, and the mixture was stirred for 45 min. A total of 42.2 mmol (3 g) of AAm was gradually introduced into the reaction mixture, followed by continuous stirring at 50 °C for an additional 20 min. A 25 mL (5% (*w/v*)) borax solution was added dropwise as a crosslinking agent, strengthening the polymer network by forming stable linkages between XG chains. The reaction was maintained at 60 °C for 4 h to complete the graft-copolymerization and crosslinking process. The resulting PAAm-*grafted*-XG hydrogel was isolated by pouring the reaction mixture into 250 mL of ethanol, inducing precipitation. The crude PAAm-grafted-XG hydrogel was purified by sequential washing steps. First, the hydrogel was repeatedly washed with distilled water to dissolve and remove any unreacted monomer and water-soluble polyacrylamide homopolymer. Subsequently, the product was precipitated in excess ethanol, in which the grafted copolymer network remains insoluble while the soluble homopolymer diffuses into the solvent phase. This purification procedure effectively eliminates unreacted species and ensures the isolation of the pure grafted hydrogel. Finally, the grafted copolymer hydrogel was dried in a vacuum oven at 50 °C. The grafting efficiency percentage was calculated to be 78%, calculated using the following equation [19]:

$$\%\text{Grafting Efficiency} = \frac{W_1}{W_2} \times 100 \quad (1)$$

where W_1 and W_2 are the weights of grafted PAAm and employed AAm, respectively.

2.2.4. Preparation of magnetic XG-grafted-PAAm

The magnetic hydrogel was prepared similarly to the XG-*grafted*-PAAm, with the key difference that after the addition of acrylamide and stirring for 30 min, 0.50 g pre-synthesized Fe_3O_4 magnetic nanoparticles (dispersed in 10 mL water using ultrasound) were added to the reaction mixture. This allowed the magnetic nanoparticles to integrate into the hydrogel network during the completion of the polymerization process.

2.2.5. Preparation of magnetic XG-grafted-PAAm@Cu-BTC nanocomposite hydrogel

For the preparation of this nanocomposite, the Cu-BTC was simultaneously formed within the magnetic hydrogel matrix. For this, 1.36 mmol (0.328 g) of Cu $(NO_3)_2.3H_2O$ and 0.84 mmol (0.176 g) of Trimesic acid were dissolved in a mixture of DMF, ethanol, and distilled water in equal proportions, with a total solvent volume of 9 mL. The solution was stirred for 20 min, after which 1 g of magnetic XG-*grafted*-PAAm hydrogel was added and stirred for an additional 20 min. The reaction was carried out in a 50 mL Teflon-lined reactor, which was sealed and heated to 80 °C for 24 h. After decanting the hot mother liquor and rinsing with DMF, the product was soaked in methanol, with the solvent replaced three times during this period. The preparation process of the XG-*grafted*-PAAm@Cu-BTC nanocomposite is illustrated in Fig. 1.

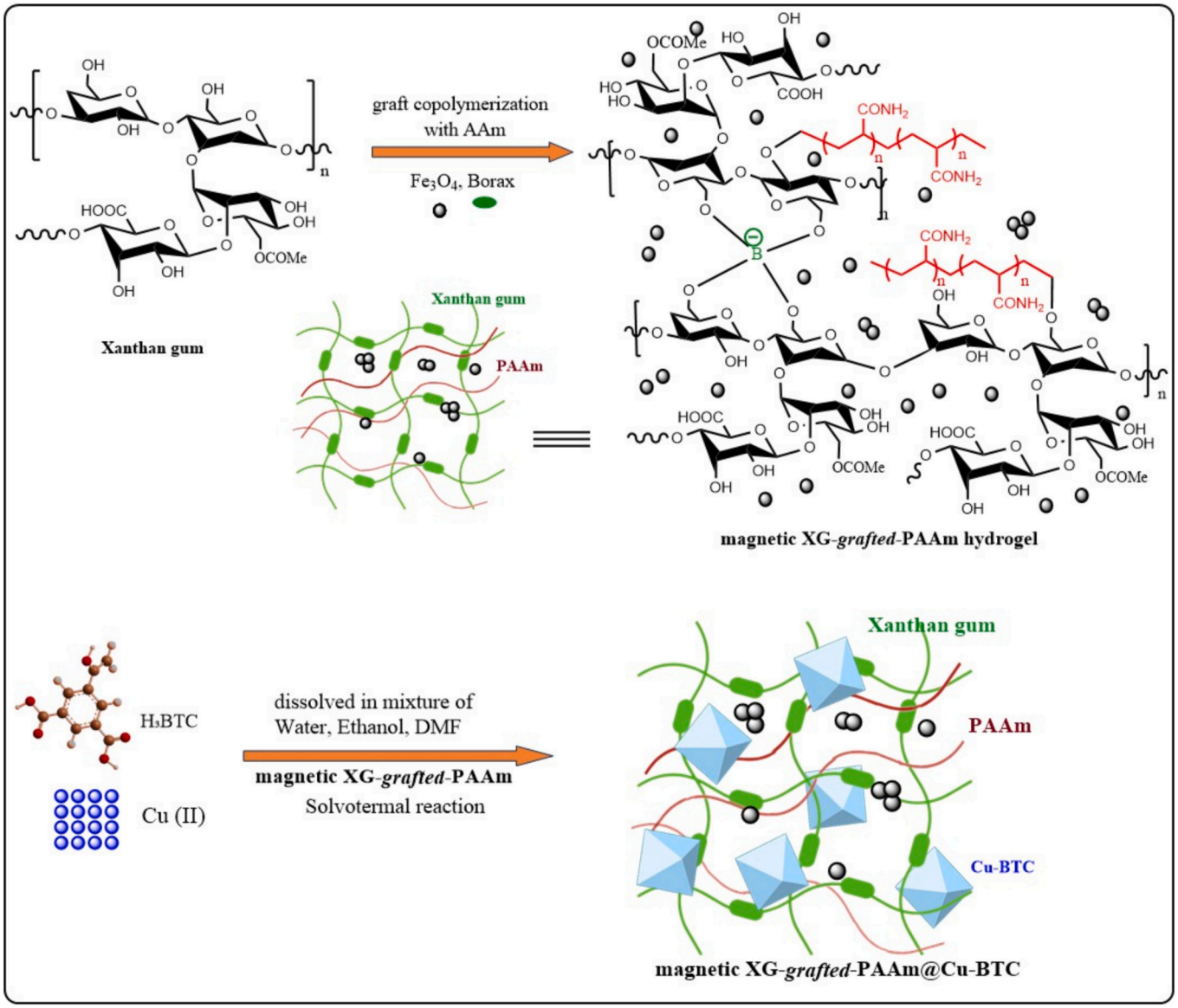

Fig. 1. The preparation pathway of the magnetic XG-*grafted*-PAAm hydrogel and magnetic XG-*grafted*-PAAm@Cu-BTC nanocomposites.

2.3. Antibacterial activity) evaluation of MIC and MBC)

The antibacterial activity of Cu-BTC MOF and XG-*grafted*-PAAm@Cu-BTC nanocomposite was assessed using the standard broth microdilution method. Pure cultures of *Escherichia coli* ATCC 25922 and *Staphylococcus aureus* ATCC 25923 were inoculated into Mueller-Hinton broth and incubated at 37 °C for 24 h. The bacterial suspensions were then standardized to a 0.5 McFarland standard. In a 96-well microtiter plate, serial dilutions of the test compounds were prepared, with each concentration tested in duplicate. Positive controls (growth medium with microbial suspension), negative controls (growth medium only), and antibiotic controls (growth medium with microbial suspension and gentamicin) were included. The microbial suspension was added to all wells except the negative controls. After 24 h of incubation, the lowest concentration without visible turbidity was recorded as the Minimum Inhibitory Concentration (MIC). To determine the Minimum Bactericidal Concentration (MBC), aliquots from the MIC well and higher concentration wells were cultured onto Mueller-Hinton agar plates and incubated at 37 °C for 24 h. The lowest concentration showing no bacterial growth on the agar was recorded as the MBC.

2.4. In vitro cytotoxicity (MTT) assay

Cell viability was evaluated using the MTT assay. L929 fibroblast cells were thawed, transferred into culture flasks containing complete Dulbecco's Modified Eagle Medium (DMEM,(containing 10% Fetal Bovine Serum)FBS(, 1% penicillin–streptomycin, and incubated at 37 °C with 5% CO_2 and 90% humidity, with medium changes every 2–3 days. For the assay, cells were seeded in 96-well plates at a density of 1×10^4 cells/well in 100 μL complete medium and incubated for 24 h at 37 °C, allowing cell attachment. After removing the medium, cells were treated with 130 μL of the prepared sample concentrations (in complete medium containing 10% FBS and 1% penicillin–streptomycin) in triplicate. Negative (medium only) and positive (10% DMSO) controls were included. After 48 h of exposure, 100 μL of MTT solution (0.5 mg/mL) was added to each well, and plates were incubated for 4 h. The medium was removed, and formazan crystals were dissolved by adding 100 μL DMSO and shaking for 15 min at 37 °C. Absorbance was measured at 570 nm using a microplate reader, and cell viability (%) was calculated relative to the negative control. All experiments were performed in triplicate, and results are reported as mean ± SD.

2.5. Cell migration (scratch) assay

The influence of the magnetic XG-*grafted*-PAAm@Cu-BTC nanocomposite on fibroblast migration was evaluated using a standard scratch assay. L929 fibroblast cells were seeded at a density of 8×10^4 cells per well in 24-well plates and allowed to grow for three days until a uniform, confluent monolayer was formed. A linear wound was then generated using a sterile 100-μL pipette tip, and detached cells were removed by gently washing the wells twice with sterile PBS. Subsequently, 500 μL of complete DMEM (10% FBS, 1% penicillin–streptomycin) containing the nanocomposite at a concentration of 3.9 μg/mL, determined based on the cytocompatibility results, was added to each well. All treatments were performed in quadruplicate. Wells containing complete medium without the nanocomposite served as the negative control. Cell migration into the scratched area was monitored by phase-contrast microscopy at 0, 6, 24, 48, and 72 h. Images were analyzed to quantify the wound width at each time point, and the percentage of wound closure was calculated relative to the initial scratch area. This assay enabled the assessment of whether the nanocomposite could promote fibroblast motility, a key parameter in the wound-healing process.

2.6. Swelling test

The swelling behavior of the dried hydrogel samples was evaluated. Pre-weighed samples (100 mg), previously dried to constant mass, were immersed individually in an excess of distilled water (50 mL) at 25 °C. At predetermined intervals (0.5–72 h), samples were withdrawn, briefly blotted with filter paper to remove surface moisture, and immediately weighed. Swelling capacity was calculated as:

$$\frac{W_s - W_d}{W_d} \times 100 \quad (2)$$

where W_d and W_s represent the dry and swollen masses, respectively. All measurements were performed in triplicate, and the swelling values were reported as mean ± standard deviation ($n = 3$).

Swelling behavior in saline solutions was evaluated. Dried hydrogel samples (100 mg; n = 3) were weighed (Wd) and immersed individually in 10 mL of PBS (pH 7.4) containing different concentrations of NaCl (0, 0.01, 0.10, 0.154, 0.50, and 1.00 M) at 25.0 °C. Samples were incubated without agitation; at 24 h (equilibrium) each sample was removed, lightly blotted once with lint-free paper to remove surface water, and immediately weighed to obtain Ws. The swelling ratio (%) was calculated. All conditions were tested in triplicate, and results are reported as mean ± SD. To avoid significant changes in the medium composition, the volume of solution per sample was chosen large enough (≥100 mL g^{-1} dry hydrogel), and solutions were freshly prepared for each condition.

Swelling experiments at different pH values were performed. Dried samples (100 mg; $n = 3$) were accurately weighed (Wd) and immersed in 10 mL of buffer solution at 25.0 °C under static conditions. Three physiologically relevant pH environments were selected: pH 5.5 (acetate buffer, 0.1 M) to simulate the mildly acidic surface of healthy skin; pH 7.4 (PBS, 1×) to represent normal physiological neutrality; and pH 4.0 (citrate buffer, 0.1 M) to mimic the acidic microenvironment characteristic of infected or inflamed wounds. After 24 h, when equilibrium swelling was reached, samples were gently removed, surface water was removed by lint-free filter paper, and the swollen weight (Ws) was recorded. The swelling ratio was calculated.

3. Results and discussion

In the present study, the multifunctional nanocomposite hydrogels, the magnetic XG-grafted-PAAm@Cu-BTC, designed as a potential material for wound healing applications, rely on the synergistic integration of Xanthan gum as a natural polymer, PAAm as a synthetic polymer, Fe_3O_4 as an inorganic magnetic nanomaterial, and functional MOFs. Xanthan gum provides a biocompatible, hydrophilic scaffold that supports moisture retention and cell compatibility, while grafting polyacrylamide enhances functionality and facilitates a uniform, interconnected network suitable for cell migration. Borax, as a mild and non-toxic crosslinker, creates dynamic borate, reinforce the network while maintaining flexibility, properties important for wound conformability. Incorporating Fe_3O_4 nanoparticles during the polymerization process further enriches the hydrogel with magnetic responsiveness and catalytic activity; these nanoparticles can interact with hydroxyl, carboxyl, and amide groups through hydrogen bonding, electrostatic attractions, stabilizing them within the 3D network and decreasing agglomeration. Such a magnetic inclusion also enables localized regulation of ROS generation and enhances antimicrobial performance, both important factors in treating an infected wound. Upon this magnetic hydrogel framework, the in-situ growth of Cu-BTC MOF with magnetic hydrogel yields distributed crystallites intimately anchored within the polymer network. This synthesis strategy, driven by the coordination of Cu^{2+} ions with functional groups on the hydrogel followed by BTC-induced crystallization, ensures strong interfacial compatibility, condenses aggregation, and improves hydrolytic stability compared to simple mixing and blending approaches. The presence of Cu-BTC introduces sustained Cu^{2+} release and enhances reactive oxygen species (ROS) generation, contributing to the antibacterial efficacy confirmed through MIC and MBC analyses. Importantly, embedding Cu-BTC within a natural-polymer hydrogel matrix is expected to modulate copper-ion release and reduce direct cellular exposure, thereby potentially lowering cytotoxicity relative to free MOF particles, a key advantage for biomedical use. Overall, this integrated design provides a substance for subsequently evaluating antibacterial performance, cytocompatibility, and cell migration behavior to determine the hydrogel's suitability as an advanced wound-dressing material.

3.1. Characterization

3.1.1. Fourier-transform infrared (FT-IR) spectroscopy

FT-IR spectroscopy was employed to identify functional groups and confirm the formation of desired functional moieties during different stages of a reaction, providing evidence for successful chemical modifications. The FTIR spectra of (a) Fe_3O_4 MNPs, (b) XG, (c) XG-*grafted*-PAAm (d), Cu-BTC (e), and magnetic XG-*grafted*-PAAm@Cu-BTC were recorded in the range of 4000–400 cm^{-1}. Samples were prepared using the KBr pellet method, and the resulting spectra are presented in Fig. 2. In spectrum (b), a characteristic peak was observed at 1023 cm^{-1} corresponding to the C–O–C bond group in XG, respectively. Additionally, the asymmetric and symmetric stretching vibrations of carboxylate groups appeared at 1624 cm^{-1} and 1464 cm^{-1}. The stretching vibrations of C—H bonds were noted in the range of 2918–2866 cm^{-1}, while a broad absorption band at 3425 cm^{-1} indicated the presence of O—H stretching vibrations [20]. Spectrum (a) belongs to Fe_3O_4 MNPs, displaying a characteristic Fe—O stretching vibration at 563 cm^{-1}. Spectrum (c) corresponds to the XG-*grafted*-PAAm hydrogel, highlighting the structural changes resulting from the graft copolymerization of acrylamide monomers onto XG polymeric chains [21]. This stage was followed by the introduction of borax; borax was then introduced as a crosslinker, forming borate ester linkages with XG hydroxyl groups. The FT-IR spectrum shows a broad band at 3000–3500 cm^{-1} due to overlapping N—H (PAAm) and O—H (XG) stretching vibrations, while peaks at 1412 and 1670 cm^{-1} correspond to C—N and C═O of PAAm. The absence of C═C bands around 1600–1620 cm^{-1}, along with shifts in C═O and C—N, confirms that PAAm is covalently grafted onto XG rather than present as free homopolymer or physical mixture. As mentioned in the experimental section, the hydrogel was further purified by washing with water and ethanol to remove unreacted monomer and soluble homopolymer, ensuring isolation of the pure grafted

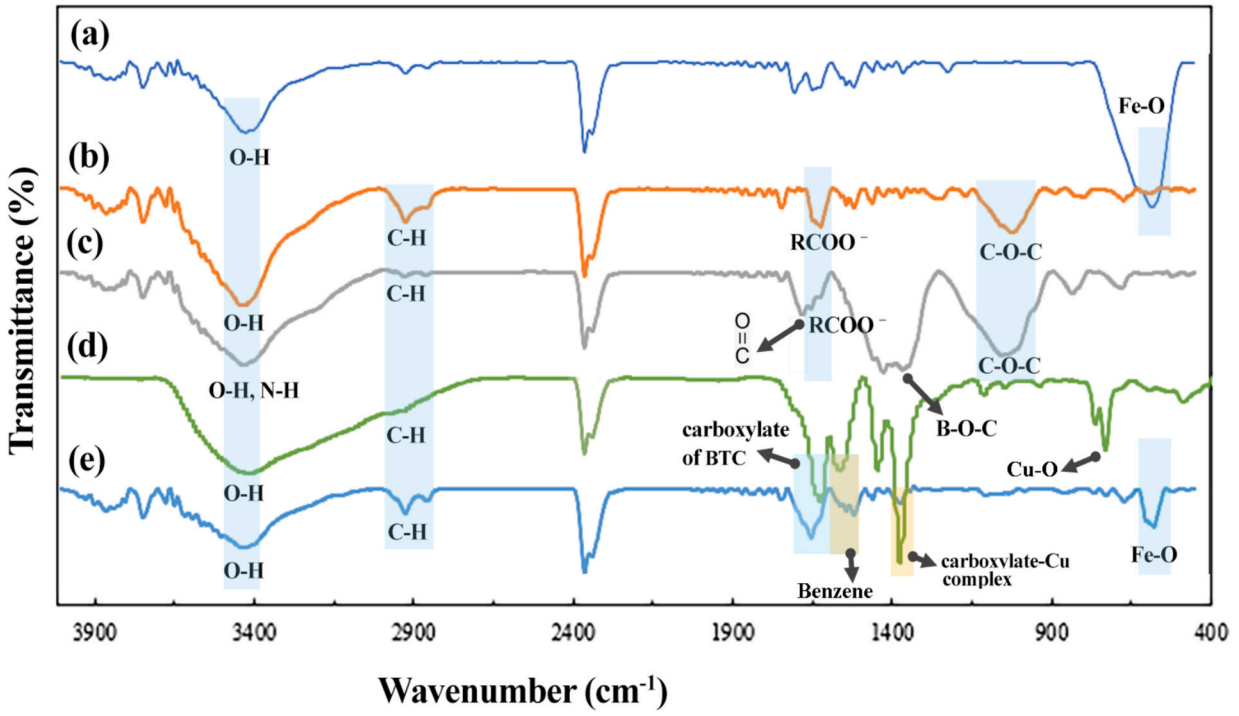

Fig. 2. The FT-IR spectra of (a) Fe_3O_4 MNPs, (b) XG, (c) XG-*grafted*-PAAm, (d) Cu-BTC, and (e) magnetic XG-*grafted*-PAAm@Cu-BTC.

hydrogel. The spectrum (d) shows a broad absorption band in the 2500–3300 cm^{-1} region, corresponding to O—H stretching vibrations, indicative of loosely bound water molecules within the framework. The asymmetric and symmetric stretching vibrations of the carboxylate (COO^-) groups of the benzene-1,3,5-tricarboxylate (BTC) linker are observed at 1620 and 1370 cm^{-1}, respectively, confirming coordination with Cu^{2+} ions and deprotonation of the COOH groups. Vibrations of the benzene rings appear around 1570 cm^{-1}. A band at 727 cm^{-1} is attributed to Cu—O (metal–ligand) vibrations, providing direct evidence of metal–ligand coordination. Collectively, these spectral features confirm the successful formation of the Cu-BTC MOF [22]. The FT-IR spectrum of the magnetic XG-*grafted*-PAAm@Cu-BTC (spectrum e) reveals notable changes relative to pristine Cu-BTC, consistent with strong interactions between the MOF and the hydrogel network. In particular, the Cu—O stretching band observed in the MOF is significantly weakened in the composite, a phenomenon previously attributed to hydrogen bonding or coordination between MOF metal centers and polymer functional groups in MOF–hydrogel systems [23]. Similarly, the absorption band at ~ 1370 cm^{-1}, which corresponds to the symmetric carboxylate stretch in Cu-BTC, shows marked reduction in intensity; this can be explained by additional hydrogen bonding and coordination interactions between the carboxylate groups of the BTC linker of Cu-BTC and the hydroxyl/amide groups of the magnetic XG-*grafted*-PAAm hydrogel matrix. Such spectral behavior is in agreement with earlier reports on MOF–hydrogel composites [24].

3.1.2. Field emission scanning electron microscopy (FESEM)

FESEM provided detailed images of the surface morphology of the prepared samples. The FESEM images of the prepared samples, including (a) Fe_3O_4 MNPs, (b) XG, (c) XG-*grafted*-PAAm, (d) Cu-BTC, and (e) XG-*grafted*-PAAm@Cu-BTC, are presented in Fig. 3. XG has a non-porous morphology with relatively smooth surfaces (Fig. 3a). Fig. 3b shows the spherical shape of Fe_3O_4 MNPs, along with noticeable aggregation, which can be attributed to interparticle Van der Waals interactions. Fig. 3c, presenting the microscopic image of the XG-*grafted*-PAAm, displays significant changes compared to the unmodified XG. The entire surface of the XG exhibits alterations, which can be attributed to the graft polymerization of acrylamide onto its polymeric chains and crosslinking reaction by Borax. As is observed in Fig. 3d, Cu-BTC MOF exists in an octahedral structure with distinct edges and smooth surfaces, aligning well with previously reported findings in the literature [25]. The microscopic image of the magnetic XG-*grafted*-PAAm@Cu-BTC nanocomposite, Fig. 3e, revealed the presence of well-defined Cu-BTC MOF structures with relatively uniform micron-scale dimensions that are densely and consistently distributed in the hydrogel matrix and cover it. Furthermore, quantitative image analysis was also performed: Fe_3O_4 particle sizes were measured for 20 nanoparticles, and the edge length of 10 Cu-BTC octahedra in the final composite was recorded to obtain a size-distribution profile, which is presented in Fig. 3 e and f.

3.1.3. Atomic force microscopy (AFM)

AFM is a technique for examining the surface morphology and topographical features of materials at the nanoscale. It provides high-resolution, three-dimensional images, offering critical insights into material properties such as nucleation processes, growth mechanisms, and surface roughness [26]. AFM analysis of the magnetic XG-*grafted*-PAAm@Cu-BTC nanocomposite reveals a uniformly rough surface morphology across a 10 μm × 10 μm area, with surface heights reaching up to 150 nm) Fig. 4a). Quantitative measurements indicate an average roughness (Ra) of 16.72 nm and a root mean square roughness (Rq) of 31.89 nm, suggesting a consistent nanoscale topography. These surface characteristics are indicative of the successful integration of Cu-BTC MOF and Fe_3O_4 nanoparticles within the hydrogel matrix. Nanometer-scale roughness in this range is known to enhance protein adsorption and focal-adhesion formation, thereby facilitating early fibroblast and keratinocyte attachment [27]. Protein adsorption is highly sensitive not only to nanogeometry but also to surface chemistry and wettability. Certain nanoscale roughness patterns enhance the adsorption and conformational adaptation of adhesive proteins (e.g., fibronectin, fibrinogen), which facilitate cell adhesion [28]. Therefore, the observed Ra = 16.72 nm likely promotes protein-mediated cell anchoring on our composite, aided by polar functional groups from xanthan/PAAm and MOF/Fe_3O_4 components. In wound dressings, nanoscale roughness affects fluid handling and biological interactions. Increased roughness and

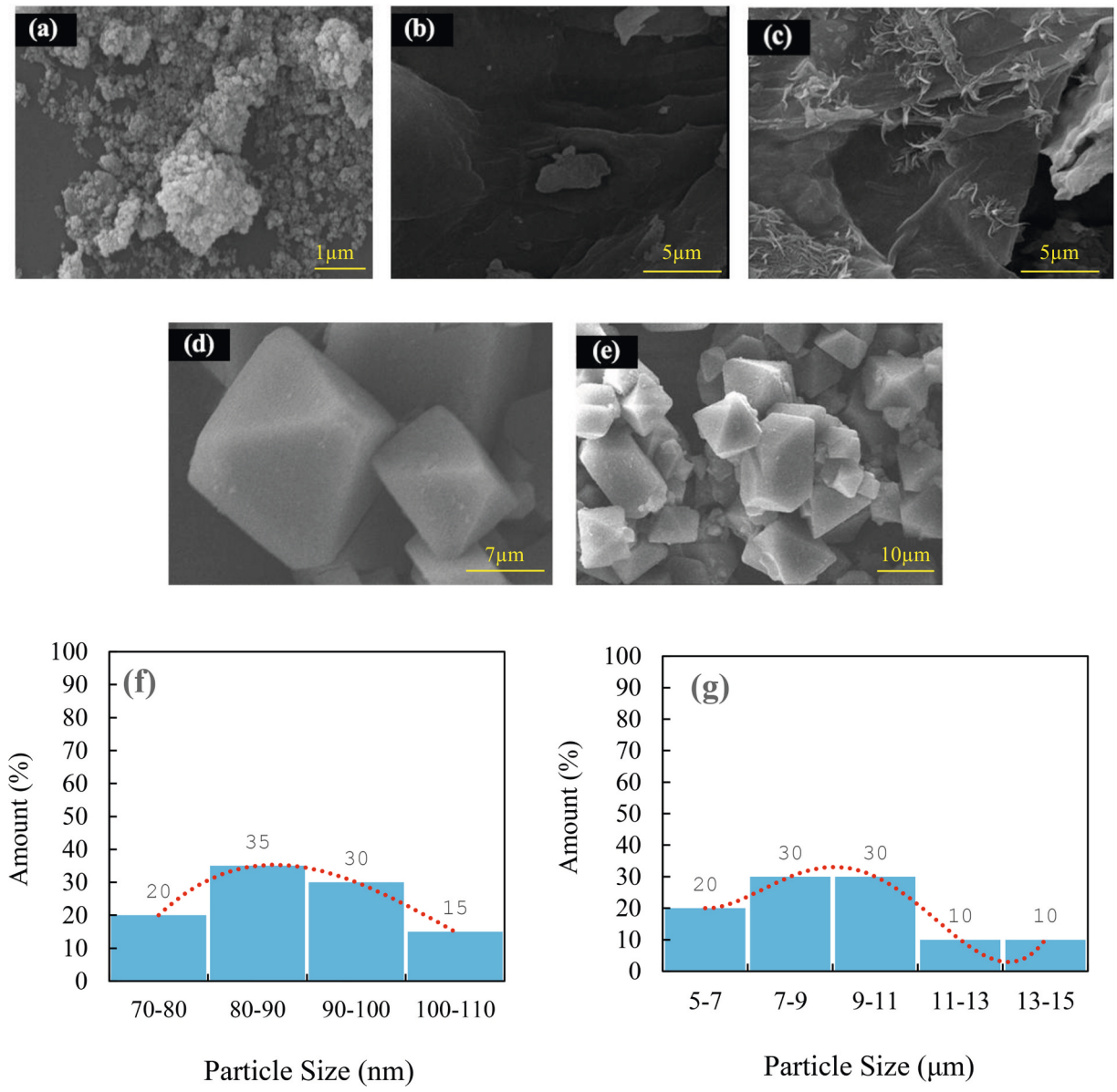

Fig. 3. The FESEM images of (a) Fe_3O_4 MNPs, (b) XG, (c) XG-*grafted*-PAAm, (d) Cu-BTC, and (e) the magnetic XG-*grafted*-PAAm@Cu-BTC nanocomposites. The diameter distribution of (f) Fe_3O_4 MNPs, (g) Cu-BTC from the nanocomposites.

nanoporosity enhance capillary uptake and retention of exudate within a hydrophilic polymer matrix, improving fluid absorption. However, roughness can also influence bacterial adhesion depending on surface chemistry [29,30]. In conclusion, the AFM data (Ra = 16.72 nm, Rq = 31.89 nm) suggest a nanoscale surface likely to support improved initial biological interactions relative to smoother surfaces.

3.1.4. X-ray diffraction (XRD)

XRD analysis is a conventional technique for investigating the structural properties of materials. The XRD pattern of Fe_3O_4 nanoparticles, Fig. 5a, displays prominent peaks at 2θ values of approximately 30.6°, 35.9°, 43.3°, 54.2°, 57.5°, and 63.3°, corresponding to the (220), (311), (400), (422), (511), and (440) crystal planes, respectively. These reflections are characteristic of the cubic spinel structure of Fe_3O_4, as documented in standard reference patterns such as JCPDS card number 01-77-0010. The absence of additional peaks in the diffraction pattern indicates the high purity of the synthesized Fe_3O_4 nanoparticles, with no detectable impurities like $Fe(OH)_3$ or Fe_2O_3, which are common by-products in the chemical co-precipitation method [31,32]. The diffractogram of xanthan gum, Fig. 5b, has a characteristic peak within the 2θ range of 15° -25°, centered around 20°, indicative of its semi-crystalline nature as noted in previous studies [33]. As can be seen in Fig. 5c, the XRD pattern of grafted copolymer, XG-grafted-PAAm, displayed distinguishable diffraction peaks at 2θ values of 8.4°, 11.7°, 19.4°, 24°, and 28.2° compared to the crude xanthan gum. This change confirms the successful grafting of acrylamide onto xanthan gum, resulting in a copolymer with enhanced crystallinity [34]. This structural modification has been observed in similar graft *co*-polymerizations, where the introduction of synthetic polymers onto natural polysaccharide backbones [35,36]. In Fig. 5d, the XRD pattern of magnetic XG-grafted-PAAm exhibits peaks corresponding to Fe_3O_4 magnetic nanoparticles, in addition to previously discussed broad features. These peaks have lower intensities, likely due to the incorporation of magnetic nanoparticles within the polymer matrix, which can attenuate their diffraction signals. [37]. The XRD pattern of Cu-BTC MOF, Fig. 5e, exhibits distinct peaks at 2θ values of approximately 6.67°, 9.5°, 11.6°, 14.62°, 16.5°, 17.5°, 19.08°, 20.25°, 21.30°, 23.45°, 24.09°, 25.96°, 27.69°, 28.74°, and 35.26°. These peaks correspond to the (200), (220),

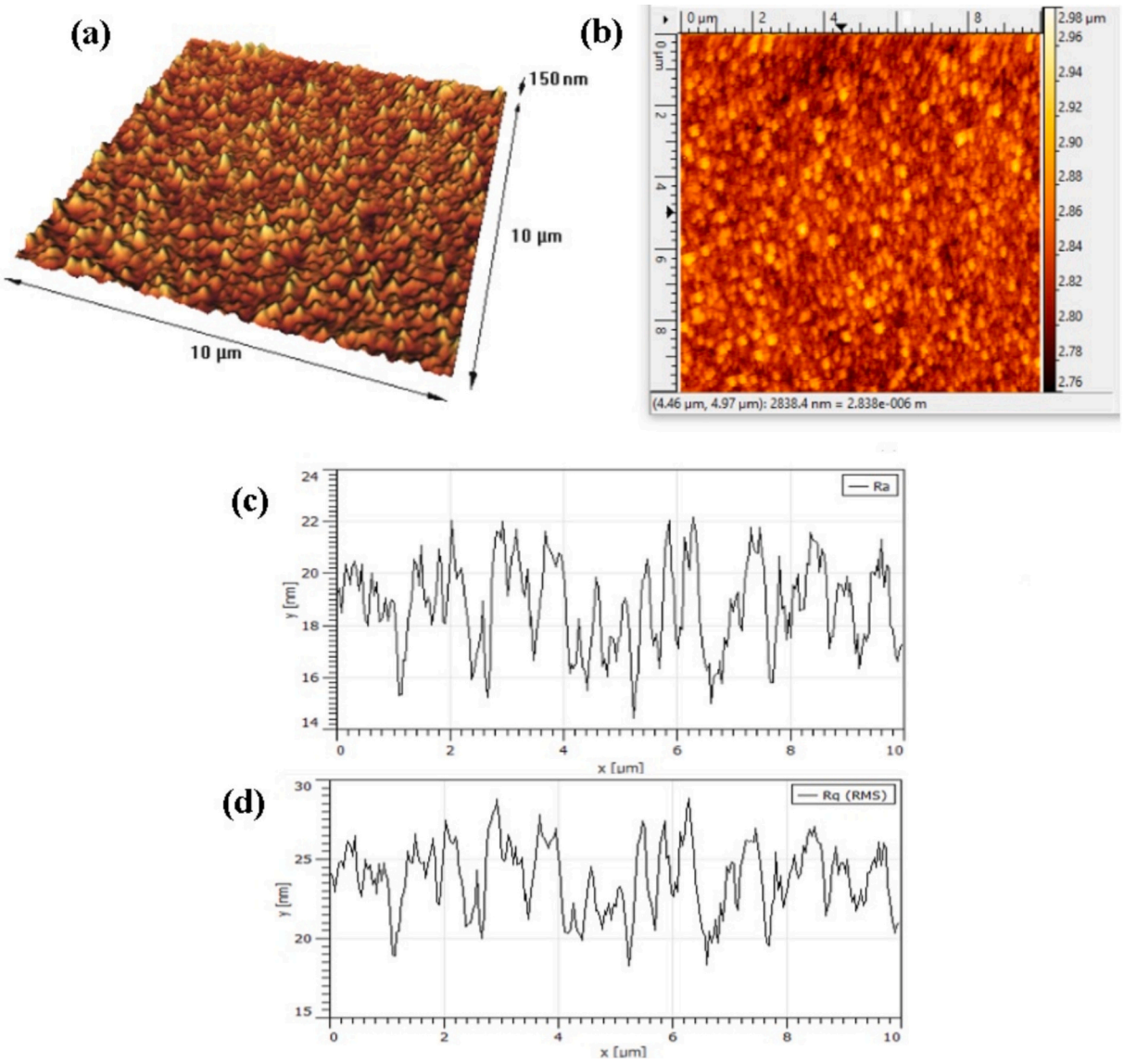

Fig. 4. (a,b) Semi-3D AFM images, (c) Ra, and (d) Rq of the magnetic XG-*grafted*-PAAm@Cu-BTC.

(222), (400), (422), (511), (440), (442), (620), (444), (551), (553), (733), and (660), and (951) crystallographic planes, respectively, matched well with the standard HKUST-1 reference pattern (ICDD pdf no. 00-062-1183) confirming the successful formation of Cu-BTC. This pattern aligns with previous reports, indicating successful synthesis of the material [38–40]. A very weak reflection near $2\theta \approx 35^{\circ}$ was also observed, which may correspond to a trace amount of CuO; however, the absence of the accompanying CuO peak at ~38.7° confirms that any oxide impurity is minimal and does not influence the structural integrity of the framework. The XRD pattern of the magnetic XG-*grafted*-PAAm@Cu-BTC composite closely resembles that of pristine Cu-BTC MOF. This similarity indicates the successful formation of Cu-BTC MOF's crystalline phase within the composite material without disrupting its structural integrity, using the in-situ synthesis approach.

3.1.5. *Vibrating sample magnetometry (VSM)*

The magnetic properties of magnetic XG-*grafted*-PAAm and magnetic XG-*grafted*-PAAm@Cu-BTC were analyzed using a VSM at 300 K (room temperature) in applied fields ranging from −10 kOe to +10 kOe with a sweep rate of 200 Oe/s. As can be observed in Fig. 6, the magnetization curves of both samples displayed the characteristic S-shape indicative of superparamagnetic behavior, marked by the absence of hysteresis loops, which is fundamental for effective magnetic field-responsive heating and reversible dispersion in liquid media [41]. The saturation magnetization (Ms) values were approximately 12 emu/g for the magnetic XG-*grafted*-PAAm and 8 emu/g for the magnetic XG-*grafted*-PAAm@Cu-BTC. The reported Ms. for Fe_3O_4 MNPs in our previous work was about 56 emu/g. The reduced Ms. in the magnetic hydrogel and magnetic composite compared to pure Fe_3O_4 MNPs. The non-magnetic polymer matrix reduces the overall magnetic content per unit mass, leading to lower Ms. values. Such reductions in Ms. are common in magnetic hydrogels, as the polymer network's non-magnetic nature and the distribution of magnetic nanoparticles within the matrix influence the composite's magnetic behavior. Such Ms. values fall well within the range reported for magnetic hydrogels successfully used in wound healing, particularly for external field-assisted placement and anchoring of magnetic dressings, as well as magneto-responsive actuation [42,43]. Previous studies have demonstrated that even relatively low saturation magnetization values (typically 3–15 $emu \cdot g^{-1}$) can provide sufficient magnetic responsiveness for biomedical applications such as wound healing and tissue regeneration. For example, Zhang et al. reported a magneto-responsive agar/tetra-PEG hydrogel incorporating Fe_3O_4 nanoparticles, which enhanced fibroblast proliferation and accelerated tissue repair under a mild external magnetic field [44]. More recently, Xuan et al. reported 3D-

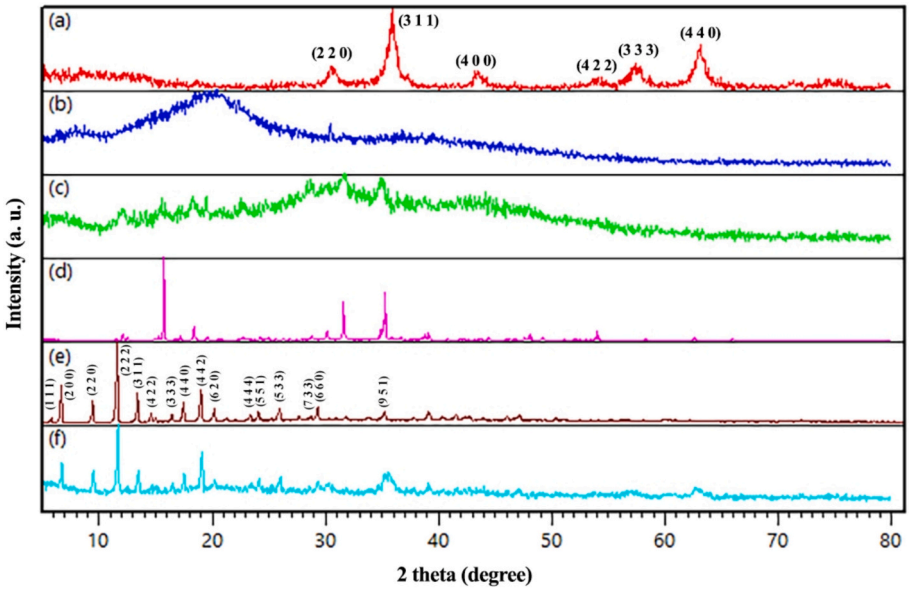

Fig. 5. The XRD diffractograms of (a) Fe_3O_4 MNPs, (b) XG, (c) XG-*grafted*-PAAm, (d) magnetic XG-*grafted*-PAAm, (e) Cu-BTC, and (f) magnetic XG-*grafted*-PAAm@Cu-BTC.

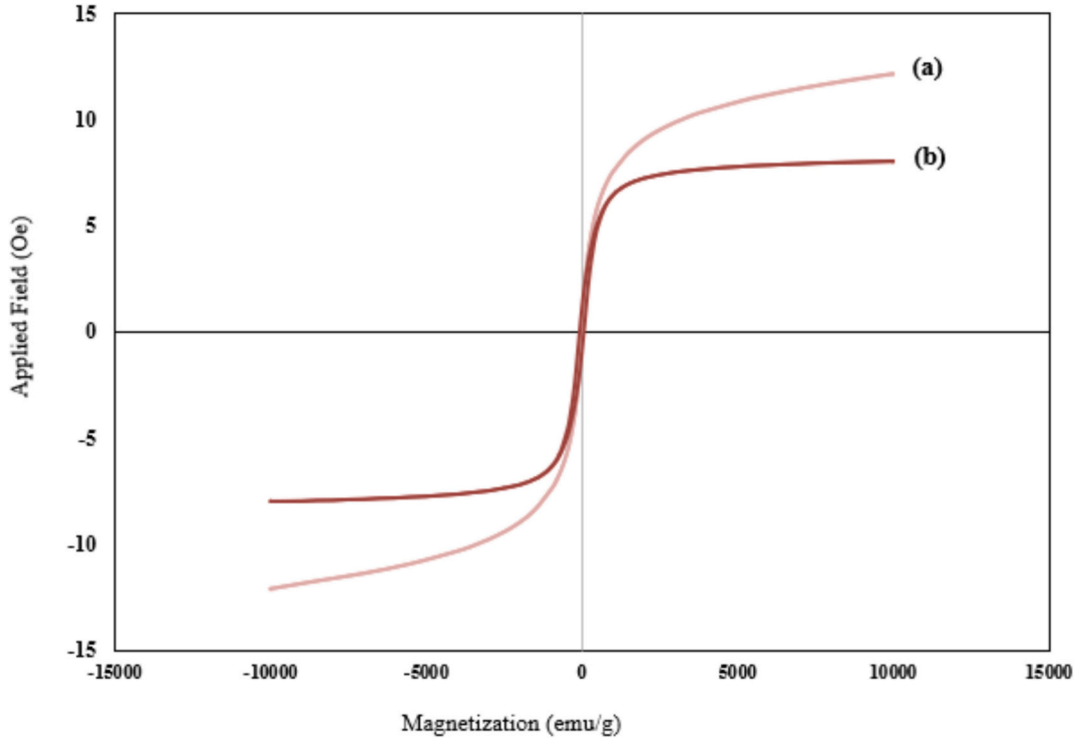

Fig. 6. The VSM of (a) magnetic XG-*grafted*-PAAm, and (b) magnetic XG-*grafted*-PAAm@Cu-BTC.

printable PAM–Fe_3O_4 hydrogels with Ms. ≈ 3.4–9.1 emu·g^{-1} (for 5–15 wt% Fe_3O_4), demonstrating clear magneto-mechanical actuation at practical field strengths, along with strong adhesive behavior on diverse substrates [45]. Chen et al. prepared PVA-based magnetic hydrogels with Ms. values between 1.3 and 5.5 emu·g^{-1}, demonstrating magnetically induced self-healing and mechanical reinforcement under external magnetic fields [46]. Liu and coworkers reviewed several Fe_3O_4-based magnetic hydrogels used in skin regeneration, reporting effective field-responsive behavior and improved cell adhesion with low Ms. values [42]. These findings indicate that the measured magnetic response in our composite is sufficient for practical wound-care applications, including external field-assisted placement and on-demand release. While the reduced Ms. may limit applications requiring strong magnetic forces at depth (e.g., in-vivo magnetic targeting or inductive hyperthermia), achieving such effects would require higher magnetic loading or particle engineering, which should be balanced against the impacts on hydrogel mechanics and biocompatibility.

3.1.6. Thermogravimetric analysis (TGA)

The thermal stability of the prepared samples, Fe_3O_4, XG, XG-*grafted*-

PAAm, magnetic XG-*grafted*-PAAm, Cu-BTC MOF, and magnetic XG-*grafted*-PAAm@Cu-BTC was studied by monitoring weight changes under controlled heating using TGA. Thermal analysis was performed by heating samples from 25 to 800 °C at 10 °C/min under N_2 flow (50 mL/min). For all samples, the first weight loss at 150–200 °C is assigned to removal of physicosorbed and pore-trapped water and residual solvents; this assignment is consistent with literature reports for Fe_3O_4 nanoparticles and porous MOFs such as Cu-BTC, where early mass loss reflects desorption of surface and framework-bound water. As can be observed in Fig. 7a, the thermogram of Fe_3O_4 exhibits 7% weight loss up to 200 °C, primarily due to the evaporation of adsorbed water and dehydration of surface hydroxyl groups. Beyond this temperature, a slight weight loss of about 5% has been observed up to 700 °C, resulting in a total weight loss of around 12% [47]. As observed in Fig. 7b. The thermal degradation profile of xanthan gum determined from combined TGA–DTG analysis reveals three well-defined decomposition stages. The DTG curve exhibits an initial moderate-intensity peak at ~100 °C, corresponding to the first mass loss of ~5% up to ~170 °C, which reflects the evaporation of physically bound water facilitated by the polymer's abundant hydroxyl (–OH) groups [48,49]. The most prominent and

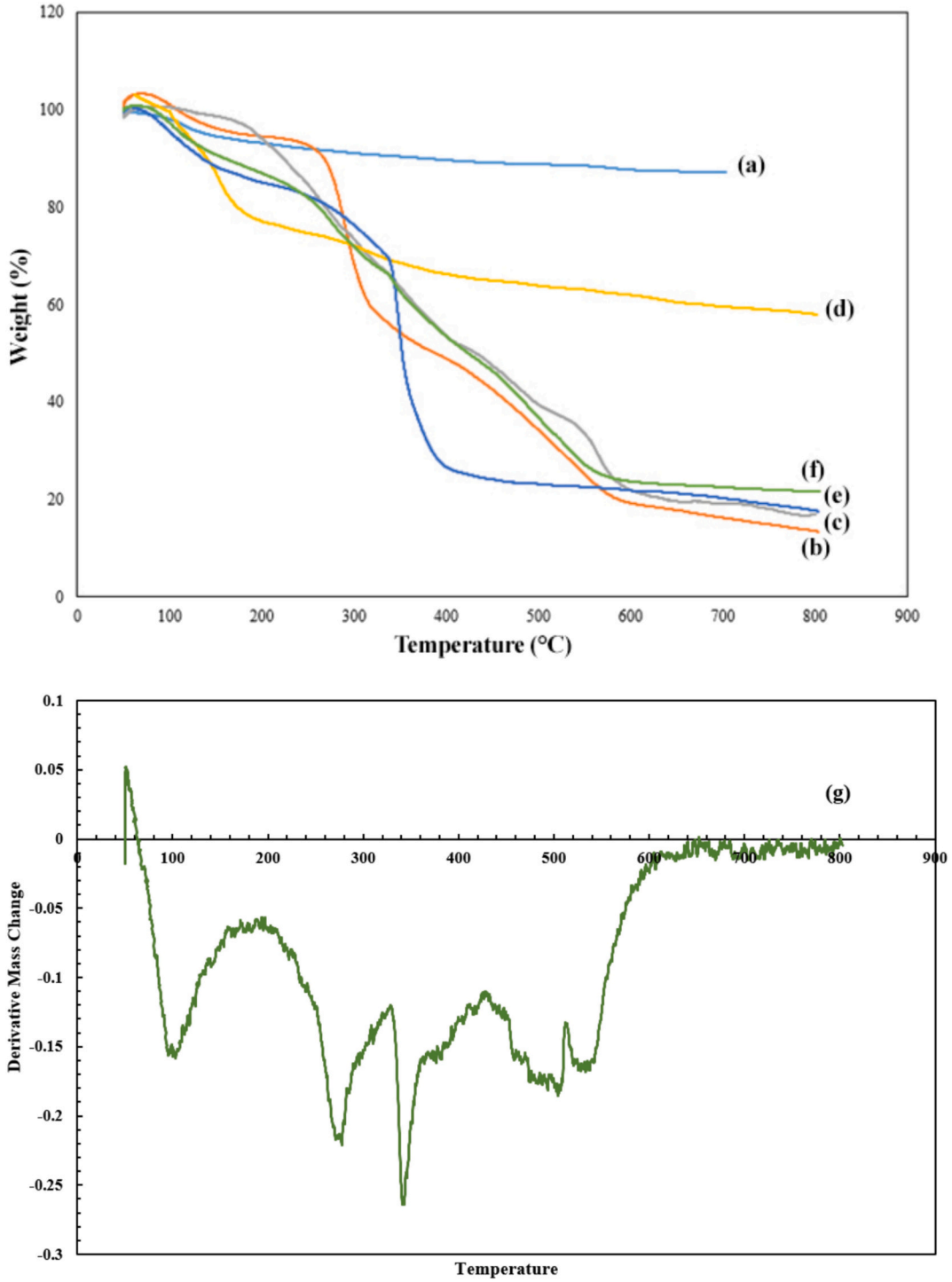

Fig. 7. The TGA curves of (a) Fe_3O_4 MNPs, (b) XG, (c) XG-*grafted*-PAAm, (d) magnetic XG-*grafted*-PAAm, (e) Cu-BTC, (f) magnetic XG-*grafted*-PAAm@Cu-BTC, and (g) DTG of the magnetic XG-*grafted*-PAAm@Cu-BTC.

sharp DTG peak appears at ~290 °C, marking the major degradation event and accounting for the principal ~45% mass loss (250,380 °C(. This stage is attributed to the depolymerization of the xanthan backbone, cleavage of side chains, and decomposition of substituent groups. A broader, medium-intensity DTG peak centered at 540 °C represents the final ~14% mass loss (400–580 °C), associated with breakdown of the main polysaccharide chain and scission of glycosidic linkages. By 800 °C, xanthan gum undergoes ~86% total weight loss, indicating extensive structural decomposition [34]. The thermal behavior of XG-*grafted*-PAAm was assessed using combined TGA/DTG analysis. The DTG curve shows three characteristic peaks: a moderate endothermic signal near ~100 °C, a sharp major peak at ~290 °C, and a broad peak around ~540 °C. These derivative features allow for a more accurate assignment of the degradation steps. The first peak (~100 °C) corresponds to loss of adsorbed/weakly bound water. The reduced intensity compared with pure xanthan gum reflects lower hydrophilicity after PAAm grafting. The major DTG peak at ~290 °C represents the principal decomposition event involving concurrent degradation of xanthan side groups and grafted polyacrylamide chains; its delayed onset relative to native XG confirms improved thermal resistance. The broad high-temperature peak (~540 °C) is associated with final breakdown of carbonaceous residues and the polysaccharide backbone. The grafted sample retains ~18% char at 800 °C, consistent with enhanced stability [50]. Overall, the result verifies that PAAm grafting modifies and stabilizes the multistep degradation pathway, shifting major decomposition to higher temperatures and improving thermal performance. Such observations are consistent with findings in related studies, where grafting synthetic polymers onto natural polysaccharides [51]. Thermogram of magnetic XG-*grafted*-PAAm, Fig. 7d, demonstrates greatly enhanced thermal stability compared to PAAm-*grafted*-XG hydrogel. Specifically, approximately 43% of the composite's weight is retained up to 800 °C, indicating significant thermal resistance. This improvement is attributed to the incorporation of Fe_3O_4 within the PAAm-*grafted*-XG hydrogel matrix, which reinforces the polymer network and hinders thermal degradation. The presence of Fe_3O_4 MNPs likely restricts the mobility of polymer chains, thereby enhancing the composite's structural integrity under elevated temperature. Such enhancements are consistent with findings in related studies [52]. As is observed in Fig. 7e, the TGA of Cu-BTC reveals a three-stage weight loss pattern. The first DTG peak at 100 °C corresponds to a ~8% mass loss associated with desorption of physisorbed water and residual solvents within the open metal–organic framework. The weight loss continued up to 340 °C, reflecting the release of coordinated water molecules and tightly trapped solvent species, confirming the hydrophilic and porous character of the MOF. The major DTG peak at 340 °C, corresponding to a substantial ~52% mass loss, marks the decomposition of the BTC linker, including decarboxylation and collapse of the Cu–carboxylate coordination network. This step produces CO_2 and ultimately yields Cu_2O/CuO residues at elevated temperatures. Consistent with previous studies, Cu-BTC retains ~15% char at 800 °C, indicating limited high-temperature stability of the framework [53–56].The TGA of the magnetic XG-*grafted*-PAAm@Cu-BTC nanocomposite, Fig. 7f, reveals a weight loss pattern similar to that of Cu-BTC MOF. Overall, the nanocomposite exhibits slightly improved thermal stability compared to magnetic XG-*grafted*-PAAm. The residual weight of the magnetic XG-*grafted*-PAAm@Cu-BTC nanocomposite until 800 °C is approximately 23%. For the nanocomposites, the enhanced stability has been mechanistically attributed to polymer– Cu-BTC and Fe_3O_4 nanoparticle interactions (e.g., restricted chain mobility and hydrogen bonding), which result in higher temperatures. The DTG profile of the magnetic XG-*grafted*-PAAm@Cu-BTC nanocomposite, Fig. 7g, reflects the rate of weight loss as a function of temperature, with each exothermic peak corresponding to a specific decomposition. The peak around 100 °C is attributed to the evaporation of physically adsorbed water and residual solvents entrapped within the hydrogel and MOF porous structures. The main peak, observed near 270 °C, likely corresponds to the degradation of loosely bound organic moieties such as side groups of xanthan gum or low molecular weight fragments of the grafted polyAcrylamide chains. The peak around 340 °C reflects partial breakdown of the polymer network. A sharper peak at 450 °C indicates major decomposition of the hydrogel matrix and MOF organic linkers, involving exothermic oxidative degradation.

3.1.7. Brunauer–Emmett–Teller (BET)

BET theory is a fundamental method to determine the specific surface area and porosity of materials. In BET analysis, an inert gas, typically nitrogen, is adsorbed onto the material's surface at liquid nitrogen temperature (77 K) [57]. The surface area and porosity were determined by N_2 adsorption-desorption at 77 K using BET analysis. Prior to analysis, samples were degassed under vacuum (Fe_3O_4: 200 °C for 4 h; Cu-BTC and others: 100 °C for 6 h) to prevent degradation. Adsorption isotherms were used to calculate surface area, pore volume, and size distribution. Table 1 presents the specific surface area, pore volume, and average pore diameter of various materials, including (a) Cu-BTC, (b) XG-*grafted*-PAAm, (c) magnetic XG-*grafted*-PAAm, and (d) magnetic XG-*grafted*-PAAm@Cu-BTC nanocomposite. As can be seen in Fig. 8, the N_2 adsorption-desorption of the nanocomposite exhibits a type I isotherm with minimal hysteresis, which is indicative of a microporous structure. Other samples show type IV curves with hysteresis loops, indicating mesoporous structures. The XG-*grafted*-PAAm sample shows a surface area of 198.82 m^2/g, a considerable increase compared to the previously reported surface area of 0.67 m^2/g for xanthan gum. This enhancement is attributed to the graft copolymerization of acrylamide onto the XG backbone, along with crosslinking by borax as an eco-friendly crosslinker and the formation of a hydrogel network, all of which contribute to the improved surface properties observed in this study. The BET surface area of magnetic XG-*grafted*-PAAm is 2.36 m^2/g, considerably lower than that of XG-*grafted*-PAAm, as the incorporation of Fe_3O_4 during the graft-copolymerization process. Among all materials, Cu-BTC MOF exhibits the highest surface area of 905.12 m^2/g due to its unique structure. The addition of the organometallic framework into magnetic XG-*grafted*-PAAm hydrogel by the in-situ growth method noticeably increases its surface area, enhancing its texture. A magnetic XG-*grafted*-PAAm@Cu-BTC nanocomposite hydrogel with a high porosity and large surface area. On the other hand, comparison with pristine Cu-BTC reveals a marked reduction in surface area, from 905.12 to 56.90 m^2/g, to be expected due to hydrogel infiltration and partial pore blockage within the MOF framework. The pronounced decrease in measured N_2-BET surface area from pristine Cu-BTC (~905 $m^2 \cdot g^{-1}$) to ~57 $m^2 \cdot g^{-1}$ for the magnetic XG-grafted-PAAm@Cu-BTC composite is consistent with numerous reports of MOF–polymer/hydrogel hybrids and can be rationalized by several non-exclusive mechanisms. First, pore blocking and pore filling by polymer chains, and crosslinkers occupy or trapped solvent during in-situ MOF growth or post-impregnation can render MOF micropores inaccessible to N_2 at 77 K, producing an apparent reduction of BET area even when the crystalline framework remains present (e.g., Cu-BTC trapped inside nanocellulose aerogels showed a drop to ~18.3 $m^2 \cdot g^{-1}$ from the expected Cu-BTC values [58]. Second, surface coverage of MOF crystals by the hydrogel matrix or by co-added nanoparticles (Fe_3O_4) reduces the accessible external surface area and pore volume without necessarily implying complete framework decomposition (examples of HKUST-1/ZIF-8 grown in gelatin or other biopolymer matrices

Table 1
BET surface area, pore volume, and pore size of Cu-BTC, XG-*grafted*-PAAm, magnetic XG-*grafted*-PAAm, and magnetic XG-*grafted*-PAAm@Cu-BTC.

Sample	Surface area ($m^2.g^{-1}$)	Pore volume ($cm^3.g^{-1}$)	Pore size (Å)
Cu-BTC	903.12	0.44	19.44
XG-*grafted*-PAAm	198.82	0.185	36.28
magnetic XG-*grafted*-PAAm	2.36	0.01	137.49
magnetic XG-*grafted*-PAAm@Cu-BTC	56.90	0.17	11.78

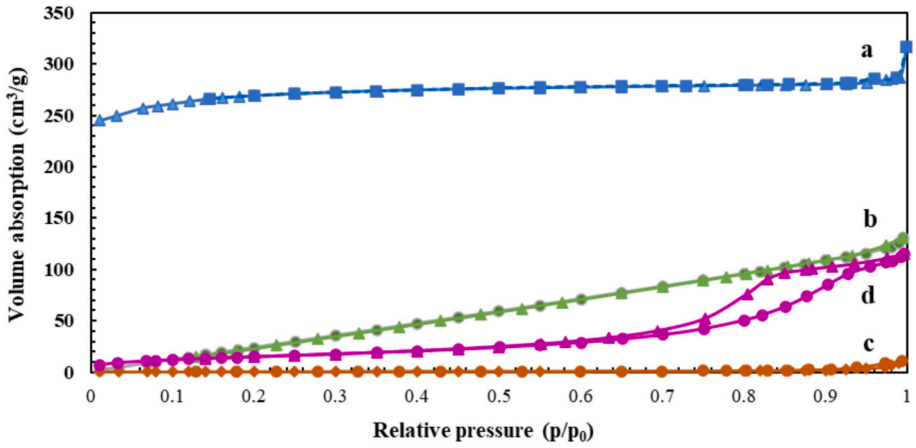

Fig. 8. The N_2 adsorption-desorption results of (a) Cu-BTC, (b) XG-*grafted*-PAAm, (c) magnetic XG-*grafted*-PAAm, and (d) magnetic XG-*grafted*-PAAm@Cu-BTC.

show strong reductions in apparent BET area attributable to polymer masking [59]. The integration of MOF particles within the polymeric hydrogel matrix alters the interfacial microenvironment in ways that enhance functionality despite the apparent reduction in N_2-BET surface area. In situ growth or embedding of MOF crystallites within the hydrogel prevents aggregation and promotes homogeneous dispersion, maintaining accessible active sites and effective surface availability in aqueous environments [60]. Although partial pore blocking may reduce drug-loading capacity by limiting available adsorption space and slightly accelerate the release rate, it can simultaneously stabilize the release profile and prevent rapid leaching of active species [61]. Strong interaction and hydrogen bonding between polymer functional groups (–OH, –COOH, $–NH_2$) and MOF nodes improve interfacial adhesion and significantly reduce MOF dissolution or metal ion leaching, leading to a more gradual and sustained release of active species [62]. Meanwhile, the hydrogel network imposes a diffusion-controlled barrier that slows adsorption/desorption kinetics, resulting in controlled and prolonged release of therapeutic or antibacterial agents through both MOF pores and the hydrated polymer matrix. These synergistic effects, stemming from steric confinement and interfacial coordination, have been consistently observed in MOF–hydrogel systems synthesized via in situ or post-integration routes.

3.2. Antibacterial activity

MOFs are innovative microporous biomaterials with diverse pharmaceutical and biological applications. They exhibit antibacterial properties through the release of metal ions (such as silver, zinc, and copper), which possess inherent antibacterial activity. Additionally, the organic ligands within MOFs may function as antibiotics or photosensitizers, generating reactive oxygen species (ROS) under light irradiation to eliminate bacteria. Furthermore, MOFs can serve as carriers for loading antibacterial agents, including antibiotics, photosensitizers, and antibacterial peptides, thereby enhancing antibacterial efficacy [63]. Importantly, the antibacterial performance of MOFs should be interpreted in comparison with other inorganic or polymeric nanomaterials rather than conventional antibiotics, because their mechanisms of action and release dynamics differ fundamentally. The antibacterial efficacy of Cu-BTC MOF, magnetic XG-*grafted*-PAAm hydrogel, and magnetic XG-*grafted*-PAAm@Cu-BTC nanocomposites was assessed through MIC and MBC evaluations at different concentrations ranging from 15.625 μg/mL to 2000 μg/mL. MIC refers to the lowest concentration of an antimicrobial agent that inhibits bacterial growth during incubation, while MBC is the minimum concentration required to kill 99.9% of the bacterial population. The MIC and MBC values of the Cu-BTC MOF, magnetic XG-*grafted*-PAAm hydrogel, and magnetic XG-*grafted*-PAAm@Cu-BTC nanocomposite for *E. coli* (Gram negative) and *S. aureus* (Gram-positive) are presented in Fig. 9 and summarized in Table 2. For the Cu-BTC MOF, both *E. coli* and *S. aureus* exhibited MIC = MBC values of 500 μg/mL and 250 μg/mL, respectively, indicating that Cu-BTC simultaneously exerts bacteriostatic and bactericidal activity at the same concentration. The MIC = MBC behavior has been widely reported for Cu-based MOFs, which rapidly disrupt bacterial membranes through oxidative stress and sustained Cu^{2+} ion release. The hydrogel exhibited a MIC of 500 μg/mL and an MBC of 2000 μg/mL against *S. aureus*, while for *E. coli*, the MIC and MBC were 500 μg/mL and 1000 μg/mL, respectively. Their antibacterial effect primarily arises from ROS generation, localized membrane perturbation, and surface charge interactions, rather than strong bactericidal metal-ion release. The MBC/MIC ratios (4 for *S. aureus* and 2 for *E. coli*) support that this hydrogel demonstrates a bactericidal effect, especially against *E. coli*. For the magnetic XG-*grafted*-PAAm@Cu-BTC nanocomposite, MIC and MBC values were 125 and 250 μg/mL against *E. coli*, and 500 and 1000 μg/mL against *S. aureus*. The MBC/MIC ratio = 2 indicates a concentration-dependent antibacterial response, bacteriostatic at MIC and bactericidal at higher concentrations [64]. Overall, comparison of the three materials clearly shows that the magnetic XG-grafted-PAAm hydrogel alone exhibits only moderate antibacterial activity, consistent with Fe_3O_4-based hydrogels whose effects mainly arise from ROS generation and membrane disturbance. In contrast, Cu-BTC MOF displays considerably stronger antibacterial performance, reflected by its lower MIC/MBC values and its characteristic MIC = MBC pattern. Incorporating Cu-BTC into the magnetic hydrogel significantly enhances antibacterial efficacy, confirming that the MOF plays the dominant role in bactericidal activity while the hydrogel matrix modulates and supports these effects.

The antibacterial behavior of Cu-BTC and its hydrogel–MOF composite (magnetic XG-grafted-PAAm@Cu-BTC) originates from multiple synergistic mechanisms. Cu-BTC provides a sustained, diffusion-controlled release of Cu^{2+} ions in aqueous media, while its redox-active copper nodes promote ROS production, including hydroxyl radicals generated through peroxidase- or Fenton-like reactions. The crystalline morphology of Cu-BTC further contributes to antibacterial action through direct physical interaction with bacterial membranes, leading to structural disruption, protein dysfunction, and leakage of intracellular components [65–67]. The hydrogel matrix further modulates these processes: it enhances the spatial dispersion of MOF particles, maintains surface exposure in hydrated media, stabilizes the local concentration of released ions, and restricts ROS diffusion, collectively promoting prolonged bactericidal activity [68]. Polymer–MOF interfacial interactions (e.g., hydrogen bonding or coordination between –OH/–COOH/$–NH_2$ groups and Cu clusters) also suppress particle aggregation and mitigate premature MOF dissolution, which is known to compromise antibacterial stability. Studies on Cu-BTC–based polymeric and hydrogel

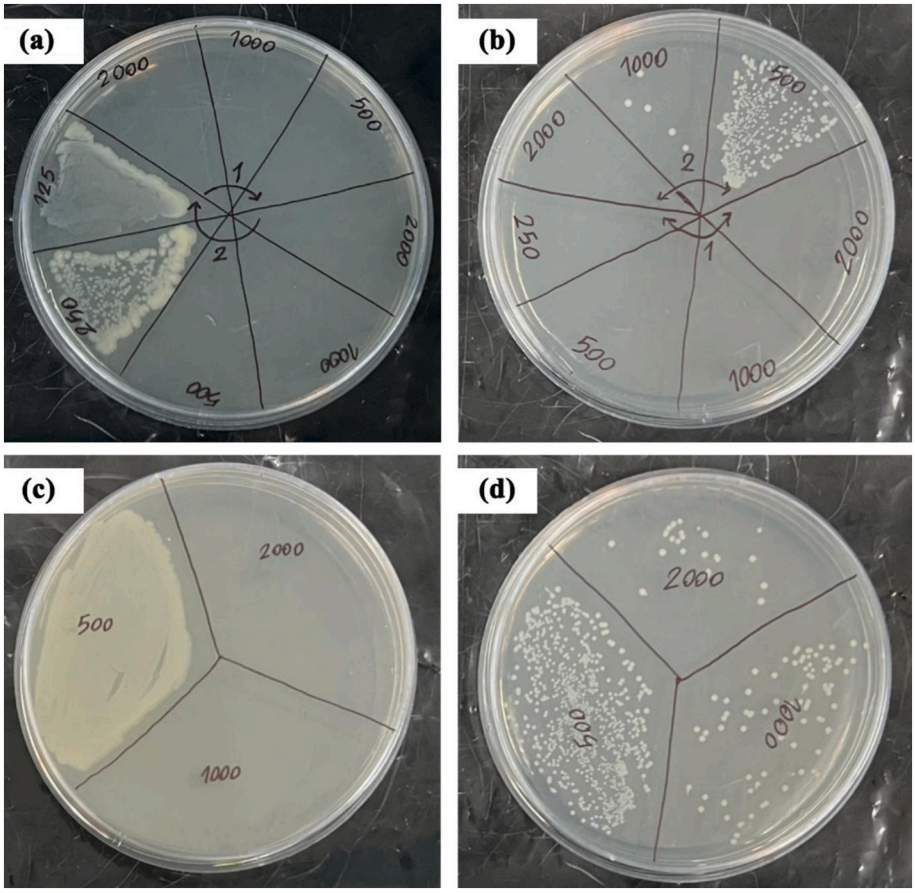

Fig. 9. The results of antimicrobial studies (MBC) of Cu-BTC MOF (sample 1), the magnetic XG-*grafted*-PAAm@Cu-BTC nanocomposite (sample 2) PAAm against (a) *E. coli* and (b) *S. aureus.*, and the magnetic XG-*grafted*- PAAm against (c) *E. coli* and (d) *S. aureus.*

Table 2
MIC and MBC of Cu-BTC MOF and magnetic XG-*grafted*-PAAm@Cu-BTC nanocomposite.

Sample	Bacterial strain	Antibacterial activity via MIC) μg/mL(	Antibacterial activity via MBC) μg/mL(
Cu-BTC MOF	*E. coli*	500 ± 10	500 ± 10
	S. aureus	250 ± 10	250 ± 10
Magnetic XG-*grafted*-PAAm	*E. coli*	500 ± 15	1000 ± 15
	S. aureus	500 ± 15	2000 ± 15
Magnetic XG-*grafted*-PAAm@Cu-BTC	*E. coli*	125 ± 12	250 ± 12
	S. aureus	500 ± 12	1000 ± 12
Gentamicin	*E. coli*	0.312 ± 0.2	–
	S. aureus	0.156 ± 0.2	–

composites consistently show that such structural integration strengthens antibacterial efficacy through synergistic contributions from ion release, ROS generation, membrane disruption, and matrix-controlled diffusion phenomena.

Furthermore, the antibacterial results reveal a clear dependence on bacterial cell-wall architecture. In the free Cu-BTC MOF, *S. aureus* (Gram-positive) showed lower MIC/MBC values than *E. coli*, indicating higher susceptibility, which is consistent with the ability of Cu^{2+} ions and ROS to diffuse through its thick but highly porous peptidoglycan layer. In contrast, for the hydrogel alone, the MIC values were identical for both strains, but the MBC values were lower for *E. coli*, reflecting its thinner peptidoglycan layer and outer membrane that is more vulnerable to ROS-mediated disruption. In the final magnetic XG-*grafted*-PAAm@Cu-BTC nanocomposite, *E. coli* displayed lower MIC/MBC values than *S. aureus*, demonstrating that the composite interacts more efficiently with Gram-negative bacteria. This shift arises because embedding the MOF inside the hydrogel matrix. The multilayered, highly crosslinked peptidoglycan matrix of Gram-positive *S. aureus*, enriched with teichoic acids, forms a dense barrier that limits the diffusion of Cu^{2+} ions and ROS generated by the Cu-BTC–embedded hydrogel. Overall, these results confirm that the enhanced antibacterial performance of the magnetic XG-*grafted*-PAAm@Cu-BTC nanocomposite is governed by synergistic ROS generation, controlled Cu^{2+} release, and the differential permeability of Gram-positive and Gram-negative cell envelopes.

In this study, we evaluated the antibacterial properties of two prepared samples, Cu-BTC MOF and magnetic XG-*grafted*-PAAm@Cu-BTC nanocomposite, against *E. coli* and *S. aureus*. MIC and MBC values for the nanocomposites were compared with those of other MOFs and MOF-based materials reported in the literature (Table 3). These materials have shown varying antibacterial activities, indicating that the synthesized nanocomposites exhibit comparable or satisfactory antibacterial activity to other MOF-based materials. In comparison with previously reported MOF-based antibacterial systems (Table 3), the magnetic XG-*grafted*-PAAm@Cu-BTC nanocomposite developed in this study demonstrates enhanced antibacterial performance. While pristine Cu-BTC is known to exert strong bactericidal activity mainly through Cu^{2+}-mediated membrane disruption, its practical efficacy is often limited by particle aggregation and rapid, burst-type metal-ion release [69]. Systems such as BioMIL-5, Zn- or Mg-based MOFs, and MOF-5 based drug carriers show moderate activity primarily governed by metal-ion release or antibiotic loading [60,70]. In contrast, our composite benefits from the homogeneous embedding of Cu-BTC (by in-situ growth) within the hydrophilic grafted-polysaccharide network, which improves dispersion, stabilizes the MOF structure, and enables controlled Cu^{2+} release

Table 3
The summary of previous studies for MOF-based nanocomposites as antibacterial nanomaterials.

Sample	Synthesis method	Testing methods	Drug	Bacterial strain	MIC (μg/mL)	MBC μg/mL	Ref.
BioMill-5	hydrothermal	Broth microdilution (CLSI-based)	–	*S. aureus*	4300	1700	[72]
CMC/MOF-5/GO@Tet	In-situ *Assembly (by Solvothermal)*	*Broth microdilution*	*Tetracyclin*	*S. aureus* *E. coli*	500 1000	–	[73]
nMOF/drug (MOF-5, IRMOF-3, Zn-BTC)	*precipitation*	*broth microdilution (CLSI)*	*Ampicillin, kanamycin*	*S. aureus*	IRMOF-3: 100 MOF-5: 200 Zn-BTC: 200	–	[74]
	Solvothermal	*broth microdilution (CLSI)*		*E. coli*	IRMOF-3: 100 MOF-5: 200 Zn-BTC: 150		
Cu-BTC Cu- gallate -MOF	*Solvothermal*	*Broth microdilution*	–	*E. coli*	1500 2000	–	[67]
Cu-BTC MOF	*Solvothermal*	*broth microdilution (CLSI-based)*	–	*E. coli* *S. aureus*	500 250	500 250	This work
Magnetic XG-*grafted*-PAAm@Cu-BTC	*Solvothermal*	*broth microdilution (CLSI-based)*	–	*E. coli* *S. aureus*	125 500	250 1000	This work

and ROS generation. The presence of Fe_3O_4 further contributes to catalytic activity and enhances interactions with bacterial cells' nanocarrier [71]. These synergistic effects collectively explain the lower MIC values obtained for *E. coli* (125 μg/mL) and *S. aureus* (500 μg/mL), positioning the composite as a competitive and promising state-of-the-art antibacterial material, while also acknowledging the influence of hydrogel confinement on MBC values.

3.3. Swelling behavior

All three hydrogel systems exhibited a characteristic biphasic swelling profile, consisting of a rapid initial uptake phase followed by a slower diffusion-controlled approach to equilibrium. As observed in Fig. 10a, the XG-*grafted*-PAAm hydrogel displayed the highest swelling capacity at all time points, consistent with its relatively open network structure and high hydrophilicity. Swelling increased sharply within the first 2–4 h, during which free water rapidly diffused into the polymer matrix, driven by the osmotic gradient and the presence of numerous amide and hydroxyl groups capable of forming hydrogen bonds with water. Equilibrium was reached at approximately 8–12 h. Incorporation of Fe_3O_4 nanoparticles into the XG-*grafted*-PAAm hydrogel reduced the overall swelling ratio and slowed the swelling kinetics. The nanoparticles increase physical crosslinking and occupy free volume within the network, which decreases chain mobility and restricts network expansion. Similar reductions in swelling have been widely reported for magnetic polysaccharide hydrogels and nanoparticle-reinforced polymer networks. The hydrogel containing Cu-BTC exhibited the lowest swelling capacity and the slowest approach to equilibrium. This behavior results from a combination of additional coordination interactions between Cu^{2+} centers and polymer chains, increased effective crosslinking density, and further reduction in free network volume due to MOF incorporation. These trends align with previous reports on MOF–polymer hybrid hydrogels, which typically show restricted swelling because the rigid MOF structures act as multifunctional crosslinking points.

Swelling behavior was assessed at pH 7.4, 5.5, and 4.0, representing physiological neutrality, healthy skin, and infected/inflamed wound environments. As observed in Fig. 10b, all samples showed maximal swelling at pH 7.4 and progressively reduced swelling at pH 5.5 and 4.0 This pH-dependent trend reflects the inherent hydration behavior of xanthan gum and polyacrylamide, whose hydroxyl, amide, and limited carboxyl groups engage in extensive hydrogen bonding. The slight decrease in negative zeta potential at acidic pH also agrees with increased chain association. In the magnetic XG-*grafted*-PAAm, incorporating Fe_3O_4 nanoparticles moderately decreased swelling by occupying inner free volume and introducing additional physical crosslinking. The Cu-BTC–containing composite exhibited the lowest swelling at all pH values due to coordination interactions with Cu^{2+} centers and the rigid MOF domains acting as multifunctional crosslinkers. From a wound-healing standpoint, sufficient swelling at pH 5.5 ensures moisture maintenance on healthy skin, whereas reduced swelling at pH 4.0 yields a more compact matrix beneficial for managing exudates in infected acidic environments, demonstrating the functional adaptability of these materials.

The swelling behavior of the prepared hydrogels in saline media was examined by immersing the samples in NaCl solutions ranging from 0.01 to 1.0 M for 24 h. As illustrated in Fig. 10c, a reduction in equilibrium swelling was observed at higher salt concentrations. This response is characteristic of xanthan gum and xanthan gum-based networks, where the strongly anionic backbone ($\zeta \approx 50$ mV across pH 3–9) drives hydration at low ionic strength but becomes progressively shielded as Na^+/Cl^- counter-ions reduce electrostatic repulsion and osmotic pressure. Consequently, the polymer matrix contracts and absorbs less water. Structural differences among the composites modulate this effect: Fe_3O_4 nanoparticles introduce additional physical crosslinking and occupy free volume, lowering swelling relative to the pristine hydrogel (XG-*grafted*-PAAm), while Cu-BTC further restricts expansion through coordination interactions and rigid MOF domains that raise effective crosslink density.

3.4. In vitro cytotoxicity evaluation

Favorable cell compatibility is essential for developing safe and effective wound-dressing materials. Since pristine Cu-BTC MOF and free copper ions may show dose-dependent cytotoxicity, assessing the biocompatibility of the prepared hydrogel–MOF nanocomposite is critical. Embedding Cu-BTC within a biocompatible polysaccharide-based hydrogel matrix significantly modulates ion release, minimizes direct cellular exposure, and consequently improves overall cytocompatibility.

To verify this, the cytotoxicity of the magnetic XG-grafted-PAAm@Cu-BTC nanocomposite was evaluated using the MTT assay (on L929 fibroblast cells) following 48 h of exposure. Serial concentrations of 1.9, 3.9, 7.8, 15.6, 31.2, 62.5, and 125 μg/mL were prepared from the stock solution in complete growth medium in accordance with the applicant's protocol. The results (Fig. 11) show a clear concentration-dependent reduction in cell viability. At lower concentrations (1.9–15.6 μg/mL), the nanocomposite maintained moderate cytocompatibility, with cell viability ranging from approximately 91% to 54%. However, higher concentrations (62.5–125 μg/mL) led to a sharp decline in viability, approaching levels observed in the positive control (~1–7%),

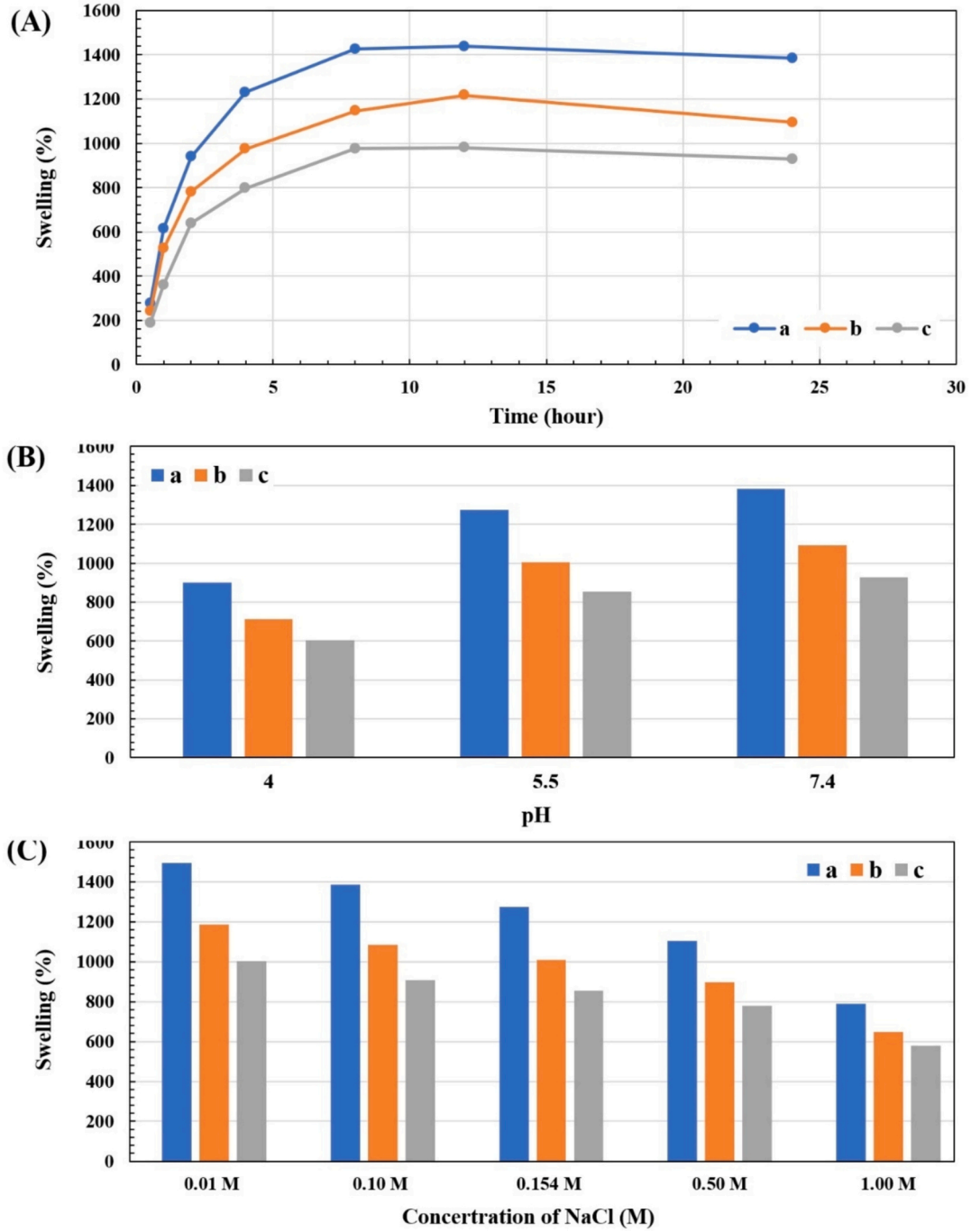

Fig. 10. (A) Time-dependent swelling of samples a, b, and c (a: XG-*grafted*-PAAm, b: magnetic XG-*grafted*-PAAm, and c: magnetic XG-grafted-PAAm@Cu-BTC). (B) Equilibrium swelling of the same samples after 24 h at pH 7.4, 5.5, and 4.0. (C) Equilibrium swelling after 24 h in NaCl solutions (0.01–1.0 M).

indicating cytotoxic effects at these doses. Extrapolating these values suggests an approximate IC_{50} (Inhibitory Concentration 50%) around ~26 μg/mL. These findings suggest that the composite is biocompatible at low-to-moderate concentrations while exhibiting dose-dependent cytotoxicity at higher levels, consistent with previously reported MOF-containing hydrogel nanocomposites. The observed concentration-dependent behavior supports careful selection of nanocomposite doses for biomedical applications to maximize antibacterial efficacy while minimizing cytotoxic effects.

3.5. *In-vitro cell migration (scratch) assay*

The scratch assay results demonstrate that treatment with the magnetic XG-*grafted*-PAAm@Cu-BTC composite (3.9 μg/mL) enhanced fibroblast migration over the 72 h period, indicating a favorable pro-healing response (Fig. 12). This trend is consistent with prior evidence on HKUST-1-based hydrogels, where incorporating HKUST-1 nanoparticles into a biocompatible polymer matrix (such as poly-(polyethyleneglycol citrate-*co*-*N*-isopropylacrylamide) (PPCN) hydrogel) enhanced cell migration and reduced Cu^{2+}-induced cytotoxicity by stabilizing the MOF structure and enabling slow, controlled ion release [68]. The improved migration observed in our study can be attributed to the moderated release of Cu^{2+} ions from Cu-BTC when embedded within the XG-*grafted*-PAAm hydrogel matrix, which reduces the inherent cytotoxicity commonly associated with free Cu-MOFs while preserving their bioactive, pro-angiogenic, and pro-migration effects. Collectively,

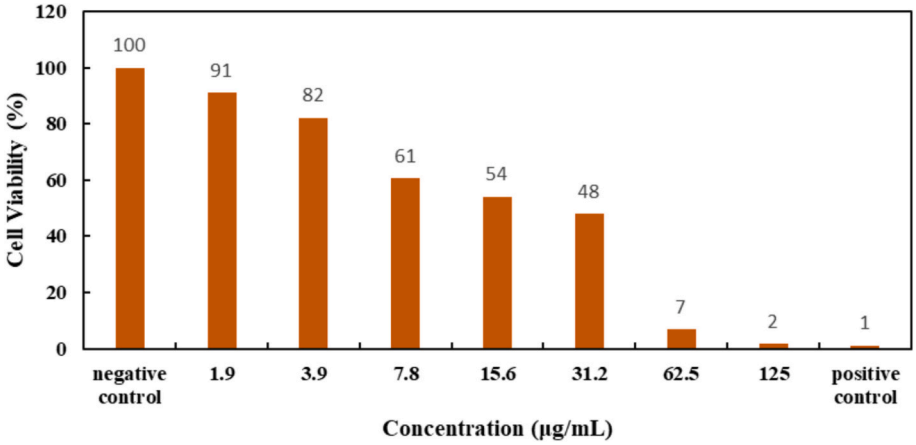

Fig. 11. The results of cell viability of L929 fibroblasts evaluated by the MTT assay in the presence of the magnetic XG-*grafted*-PAAm@Cu-BTC nanocomposite.

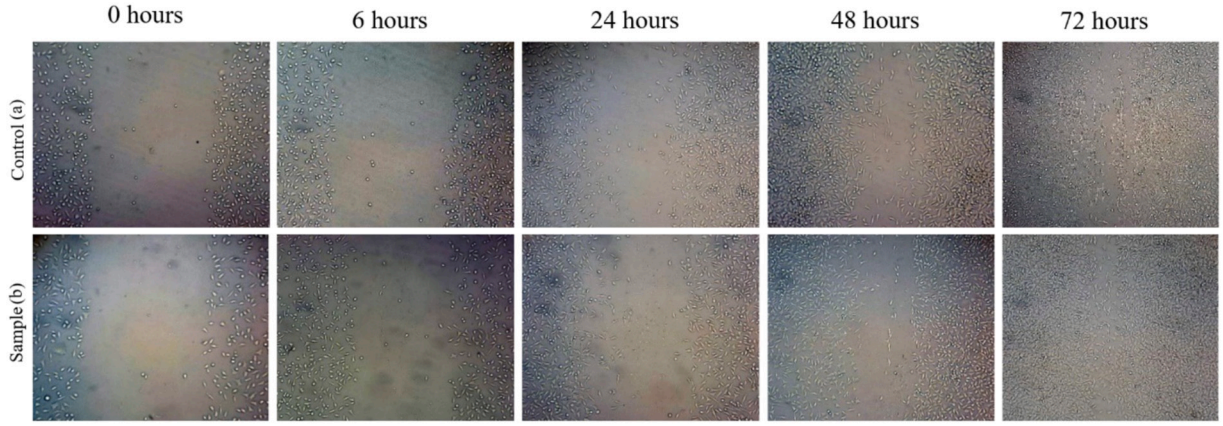

Fig. 12. Scratch assay images of L929 fibroblasts exposed to (a) control and (b) magnetic XG-*grafted*-PAAm@Cu-BTC. Representative images captured at 0, 6, 24, 48, and 72 h demonstrate differences in cell migration.

these results confirm that incorporating Cu-BTC into a hydrophilic biopolymer network not only maintains but enhances its wound-healing functionality.

4. Waste handling and disposal considerations

The environmental impact of copper-based nanomaterials must be considered alongside their biomedical applications. While copper is an essential trace element, excessive release of Cu or CuO nanoparticles into aquatic or soil environments can bioaccumulate, disrupt microbial communities, induce oxidative stress, and impair physiological functions, potentially causing long-term hazards [60,75]. In this work, the nanocomposite showed effective antibacterial activity, and in vitro cytotoxicity tests (MTT assay) confirmed good cell viability at antibacterial concentrations, indicating a safe therapeutic window. To minimize environmental risk, Waste management of all Cu-containing materials was conducted as follows: unused powders, suspensions, and contaminated consumables were collected in sealed, labeled containers. Solid waste was double-bagged or sealed in rigid containers, and liquids were stored in leak-proof vessels. Disposal followed institutional or local regulations via incineration, chemical stabilization, or transfer to licensed hazardous-waste facilities. Biosorption or chelation-based recovery of Cu^{2+} was applied where possible to minimize environmental release.

5. Conclusion

A multifunctional magnetic MOF-hydrogel nanocomposite, XG-grafted-PAAm@Cu-BTC, was successfully synthesized via in-situ growth of Cu-BTC MOF within a borax-crosslinked xanthan gum-grafted polyacrylamide hydrogel containing Fe_3O_4 nanoparticles. Characterization confirmed uniform incorporation of Fe_3O_4 and Cu-BTC, stable polymer–MOF interactions, thermal stability, and superparamagnetic behavior (~8 emu/g) with a relatively high surface area (56.9 m^2/g), providing a structurally robust and eco-friendly platform. Swelling studies showed a characteristic biphasic profile for all three hydrogels. XG-*grafted*-PAAm displayed the fastest initial water uptake and highest equilibrium swelling (~1575%), Fe_3O_4-containing hydrogel had moderate swelling (~1276%), and Cu-BTC-loaded nanocomposite exhibited the slowest uptake and lowest swelling (~1120%) due to increased crosslinking and MOF–polymer coordination. pH-dependent swelling (4.0, 5.5, 7.4) and ionic-strength tests indicated tunable hydration, supporting moisture maintenance in healthy skin and formation of compact matrices in acidic or exudative wound environments. Antibacterial testing demonstrated synergistic effects: Cu-BTC MOF alone showed MIC/MBC of 500/500 μg/mL for *E. coli* and 250/250 μg/mL for *S. aureus*, whereas XG-*grafted*-PAAm hydrogel alone exhibited moderate activity (500–2000 μg/mL). Incorporating Cu-BTC into the magnetic hydrogel significantly enhanced antibacterial performance (125/250 μg/mL for *E. coli* and 500/1000 μg/mL for *S. aureus*), attributed to combined ROS generation, controlled Cu^{2+} release, and hydrogel-mediated dispersion. Cytotoxicity assays confirmed acceptable

viability at low-to-moderate concentrations (91–54% at 1.9–15.6 μg/mL), showing that hydrogel embedding mitigates MOF-associated toxicity. Scratch-wound assays demonstrated accelerated fibroblast migration at 3.9 μg/mL, highlighting the composite's pro-healing potential. Overall, XG-*grafted*-PAAm@Cu-BTC nanocomposite offers tunable swelling, enhanced antibacterial activity, cytocompatibility, and pro-healing properties. However, the current study is limited to in vitro assessments, and the long-term biological performance, in vivo wound-healing efficacy, and potential immunogenic responses remain to be evaluated. Future work will focus on in vivo validation, optimization of MOF loading and hydrogel composition, and investigation under physiologically relevant wound conditions to facilitate clinical translation.

CRediT authorship contribution statement

Fereshte Hassanzadeh Afruzi: Writing – review & editing, Writing – original draft, Visualization, Methodology, Investigation, Formal analysis, Conceptualization. **Majid Abdouss:** Writing – review & editing, Validation, Methodology. **Sohrab Asgaran:** Methodology, Data curation. **Zahra Moazzami Goudarzi:** Visualization, Methodology. **Rasoul Esmaeely Neisiany:** Writing – review & editing, Supervision, Project administration, Funding acquisition.

Declaration of competing interest

The authors declare that they have no known competing financial interests or personal relationships that could have appeared to influence the work reported in this paper.

Acknowledgments

This work is based upon research funded by the Iran National Science Foundation (INSF) under project No. 4026014.

Data availability

Data will be made available on request.

References

[1] S. Tavakoli, A.S. Klar, Advanced hydrogels as wound dressings, Biomolecules 10 (2020) 1–20, https://doi.org/10.3390/biom10081169.
[2] M. Wang, Z. Deng, Y. Guo, P. Xu, Engineering functional natural polymer-based nanocomposite hydrogels for wound healing, Nanoscale Adv. 5 (2022) 27–45, https://doi.org/10.1039/d2na00700b.
[3] X. Lin, D. Song, T. Shao, T. Xue, W. Hu, W. Jiang, X. Zou, N. Liu, A multifunctional biosensor via MXene assisted by conductive metal–organic framework for healthcare monitoring, Adv. Funct. Mater. 34 (2024), https://doi.org/10.1002/adfm.202311637.
[4] Y. Zhong, H. Xiao, F. Seidi, Y. Jin, Natural polymer-based antimicrobial hydrogels without synthetic antibiotics as wound dressings, Biomacromolecules 21 (2020) 2983–3006, https://doi.org/10.1021/acs.biomac.0c00760.
[5] X. Zhang, M. Qin, M. Xu, F. Miao, C. Merzougui, X. Zhang, Y. Wei, W. Chen, D. Huang, The fabrication of antibacterial hydrogels for wound healing, Eur. Polym. J. 146 (2021), https://doi.org/10.1016/j.eurpolymj.2021.110268.
[6] D.F.S. Petri, Xanthan gum: a versatile biopolymer for biomedical and technological applications, J. Appl. Polym. Sci. 132 (2015), https://doi.org/10.1002/app.42035.
[7] J. Patel, B. Maji, N.S.H.N. Moorthy, S. Maiti, Xanthan gum derivatives: review of synthesis, properties and diverse applications, RSC Adv. 10 (2020) 27103–27136, https://doi.org/10.1039/d0ra04366d.
[8] S. Tang, Z. Gong, Z. Wang, X. Gao, X. Zhang, Multifunctional hydrogels for wound dressings using xanthan gum and polyacrylamide, Int. J. Biol. Macromol. 217 (2022) 944–955, https://doi.org/10.1016/j.ijbiomac.2022.07.181.
[9] J.E. Gutierrez-Reyes, M. Caldera-Villalobos, J.A. Claudio-Rizo, D.A. Cabrera-Munguía, J.J. Becerra-Rodriguez, F. Soriano-Corral, A. Herrera-Guerrero, Smart collagen/xanthan gum-based hydrogels with antibacterial effect, drug release capacity and excellent performance in vitro bioactivity for wound healing application, Biomed. Mater. 18 (2023), https://doi.org/10.1088/1748-605X/acc99c.
[10] B. Piola, M. Sabbatini, S. Gino, M. Invernizzi, F. Renò, 3D bioprinting of gelatin–xanthan gum composite hydrogels for growth of human skin cells, Int. J. Mol. Sci. 23 (2022), https://doi.org/10.3390/ijms23010539.
[11] Y.L. Fan, H.J. Liu, Z.L. Wang, Z.L. Wang, L.L. Zhu, Y.Z. Wang, F. Song, A one-Nano MOF-two-functions strategy toward self-healing, anti-inflammatory, and antibacterial hydrogels for infected wound repair, Chem. Eng. J. 497 (2024) 155037, https://doi.org/10.1016/j.cej.2024.155037.
[12] P. Dam, M. Celik, M. Ustun, S. Saha, C. Saha, E.A. Kacar, S. Kugu, E.N. Karagulle, S. Tasoglu, F. Buyukserin, R. Mondal, P. Roy, M.L.R. Macedo, O.L. Franco, M. H. Cardoso, S. Altuntas, A.K. Mandal, Wound healing strategies based on nanoparticles incorporated in hydrogel wound patches, RSC Adv. 13 (2023) 21345–21364, https://doi.org/10.1039/d3ra03477a.
[13] F. Hassanzadeh-Afruzi, M.M. Salehi, Composition States of MOFs, in: Eng. Mater., 2023, pp. 139–153, https://doi.org/10.1007/978-3-031-18675-2_10.
[14] F.H. Afruzi, M. Abdouss, E.N. Zare, E. Rezvani Ghomi, S. Mahmoudi, R.E. Neisiany, Metal-organic framework-hydrogel composites as emerging platforms for enhanced wound healing applications: material design, therapeutic strategies, and future prospects, Coord. Chem. Rev. 524 (2025) 216330, https://doi.org/10.1016/j.ccr.2024.216330.
[15] M. Zhang, D. Wang, N. Ji, S. Lee, G. Wang, Y. Zheng, X. Zhang, L. Yang, Z. Qin, Y. Yang, Bioinspired design of sericin/chitosan/ag@mof/go hydrogels for efficiently combating resistant bacteria, rapid hemostasis, and wound healing, Polymers (Basel). 13 (2021), https://doi.org/10.3390/polym13162812.
[16] C. Guo, F. Cheng, G. Liang, S. Zhang, Q. Jia, L. He, S. Duan, Y. Fu, Z. Zhang, M. Du, Copper-based polymer-metal–organic framework embedded with ag nanoparticles: long-acting and intelligent antibacterial activity and accelerated wound healing, Chem. Eng. J. 435 (2022), https://doi.org/10.1016/j.cej.2022.134915.
[17] H. Ding, L. Hao, H. Mao, Magneto-responsive biocomposites in wound healing: from characteristics to functions, J. Mater. Chem. B 12 (2024) 7463–7479.
[18] J.L.C. Rowsell, O.M. Yaghi, Effects of functionalization, catenation, and variation of the metal oxide and organic linking units on the low-pressure hydrogen adsorption properties of metal-organic frameworks, J. Am. Chem. Soc. 128 (2006) 1304–1315, https://doi.org/10.1021/ja056639q.
[19] R. Meena, K. Prasad, G. Mehta, A.K. Siddhanta, Synthesis of the copolymer hydrogel κ-carrageenan-graft-PAAm: evaluation of its absorbent and adhesive properties, J. Appl. Polym. Sci. 102 (2006) 5144–5152, https://doi.org/10.1002/app.24703.
[20] Q. Han, D. Zhang, R. Zhang, J. Tang, K. Xu, M. Shao, Y. Li, P. Du, R. Zhang, D. Yang, L. Zhang, X. Lu, DNA-functionalized metal-organic framework ratiometric nanoprobe for MicroRNA detection and imaging in live cells, Sens. Actuators B 361 (2022), https://doi.org/10.1016/j.snb.2022.131676.
[21] R. Kulkarni, B. Sa, Enteric delivery of ketoprofen through functionally modified poly(acrylamide-grafted-xanthan)-based pH-sensitive hydrogel beads: preparation, in vitro and in vivo evaluation, J. Drug Target. 16 (2008) 167–177, https://doi.org/10.1080/10611860701792399.
[22] A.L. Nuzhdin, A.S. Shalygin, E.A. Artiukha, A.M. Chibiryaev, G.A. Bukhtiyarova, O. N. Martyanov, HKUST-1 silica aerogel composites: novel materials for the separation of saturated and unsaturated hydrocarbons by conventional liquid chromatography, RSC Adv. 6 (2016) 62501–62507, https://doi.org/10.1039/c6ra06522h.
[23] Y. Li, C. Gao, J. Jiao, J. Cui, Z. Li, Q. Song, Selective adsorption of metal-organic framework toward methylene blue: behavior and mechanism, ACS Omega (2021), https://doi.org/10.1021/acsomega.1c05299.
[24] S. Elmehrath, H.F. El-Maghraby, Y.E. Greish, Enhancing the stability of cu-BTC metal-organic framework via the formation of cu-BTC@Cu3(PO4)2 MOF Core-Shell Nanoflower hierarchical hybrid composites, Adv. Mater. Interfaces (2023), https://doi.org/10.1002/admi.202300075.
[25] M.M. Salehi, F. Hassanzadeh-Afruzi, G. Heidari, A. Maleki, E. Nazarzadeh Zare, In situ preparation of MOF-199 into the carrageenan-grafted-polyacrylamide@Fe3O4 matrix for enhanced adsorption of levofloxacin and cefixime antibiotics from water, Environ. Res. 233 (2023) 116466, https://doi.org/10.1016/j.envres.2023.116466.
[26] L.D.B. Mandemaker, M. Filez, G. Delen, H. Tan, X. Zhang, D. Lohse, B. M. Weckhuysen, Time-resolved in situ liquid-phase atomic force microscopy and infrared Nanospectroscopy during the formation of metal-organic framework thin films, J. Phys. Chem. Lett. (2018), https://doi.org/10.1021/acs.jpclett.8b00203.
[27] J. Luo, M. Walker, Y. Xiao, H. Donnelly, M.J. Dalby, M. Salmeron-Sanchez, The influence of nanotopography on cell behaviour through interactions with the extracellular matrix-a review, Bioact. Mater. 15 (2022) 145–159.
[28] W. Song, H. Chen, Protein adsorption on materials surfaces with nano-topography, Chin. Sci. Bull. 52 (2007) 3169–3173.
[29] S. Zhang, L. Wang, T. Xu, X. Zhang, Luminescent MOF-based nanofibers with visual monitoring and antibacterial properties for diabetic wound healing, ACS Appl. Mater. Interfaces (2022), https://doi.org/10.1021/acsami.2c21786.
[30] N. Rani Raju, E. Silina, V. Stupin, N. Manturova, S.B. Chidambaram, R.R. Achar, Multifunctional and smart wound dressings—a review on recent research advancements in skin regenerative medicine, Pharmaceutics 14 (2022) 1574.
[31] V.E. Novala, J.G. Carriazo, Fe3O4-TiO2 and Fe3O4-SiO2 core-shell powders synthesized from industrially processed magnetite (Fe3O4) microparticles, Mater. Res. 22 (2019), https://doi.org/10.1590/1980-5373-MR-2018-0660.
[32] Q. Li, C.W. Kartikowati, S. Horie, T. Ogi, T. Iwaki, K. Okuyama, Correlation between particle size/domain structure and magnetic properties of highly crystalline Fe3O4 nanoparticles, Sci. Rep. 7 (2017), https://doi.org/10.1038/s41598-017-09897-5.
[33] N. Zhang, X. Li, J. Ye, Y. Yang, Y. Huang, X. Zhang, M. Xiao, Effect of gellan gum and xanthan gum synergistic interactions and plasticizers on physical properties of plant-based enteric polymer films, Polymers (Basel). 12 (2020) 1–13, https://doi.org/10.3390/polym12010121.

[34] F. Anjum, S.A. Bukhari, M. Siddique, M. Shahid, J. Herman Potgieter, H.Z. E. Jaafar, S. Ercisli, M. Zia-Ul-Haq, Microwave irradiated copolymerization of xanthan gum with acrylamide for colonic drug delivery, BioResources 10 (2015) 1434–1451, https://doi.org/10.15376/biores.10.1.1434-1451.
[35] V. Singh, S.K. Singh, S. Pandey, R. Sanghi, Synthesis and characterization of guar gum templated hybrid nano silica, Int. J. Biol. Macromol. 49 (2011) 233–240, https://doi.org/10.1016/j.ijbiomac.2011.04.019.
[36] R.K. Sharma, Lalita, Synthesis and characterization of graft copolymers of N-Vinyl-2-Pyrrolidone onto guar gum for sorption of Fe^{2+} and Cr^{6+} ions, Carbohydr. Polym. 83 (2011) 1929–1936, https://doi.org/10.1016/j.carbpol.2010.10.068.
[37] N. Ali, B. Zhang, H. Zhang, W. Zaman, X. Li, W. Li, Q. Zhang, Interfacially active and magnetically responsive composite nanoparticles with raspberry like structure; synthesis and its applications for heavy crude oil/water separation, Colloids Surfaces A Physicochem. Eng. Asp. 472 (2015) 38–49, https://doi.org/10.1016/j.colsurfa.2015.01.087.
[38] B. Sun, S. Kayal, A. Chakraborty, Study of HKUST (copper benzene-1, 3, 5-tricarboxylate, cu-BTC MOF)-1 metal organic frameworks for CH4 adsorption: an experimental investigation with GCMC (grand canonical Monte-Carlo) simulation, Energy 76 (2014) 419–427.
[39] K.-S. Lin, A.K. Adhikari, C.-N. Ku, C.-L. Chiang, H. Kuo, Synthesis and characterization of porous HKUST-1 metal organic frameworks for hydrogen storage, Int. J. Hydrog. Energy 37 (2012) 13865–13871.
[40] B.H. Bowser, L.J. Brower, M.L. Ohnsorg, L.K. Gentry, C.K. Beaudoin, M. E. Anderson, Comparison of surface-bound and free-standing variations of HKUST-1 MOFs: effect of activation and ammonia exposure on morphology, crystallinity, and composition, Nanomaterials (2018), https://doi.org/10.3390/nano8090650.
[41] N. Fujisawa, M. Ebara, J.J. Lai, Magnetic induction heating enables on-demand drug release via Diels–Alder polymeric nanocarriers, Biomacromolecules 26 (2025) 7265–7274.
[42] Z. Liu, J. Liu, X. Cui, X. Wang, L. Zhang, P. Tang, Recent advances on magnetic sensitive hydrogels in tissue engineering, Front. Chem. 8 (2020) 124.
[43] Z. Fan, G. Zhang, W. Zhan, J. Wang, C. Wang, Q. Yue, Z. Huang, Y. Wang, Hyaluronidase-responsive hydrogel loaded with magnetic nanoparticles combined with external magnetic stimulation for spinal cord injury repair, Mater. Today Bio 30 (2025) 101378.
[44] L. Zhang, X. Zuo, S. Li, M. Sun, H. Xie, K. Zhang, J. Zhou, L. Che, J. Ma, Z. Jia, et al., Synergistic therapy of magnetism-responsive hydrogel for soft tissue injuries, Bioact. Mater. 4 (2019) 160–166.
[45] X. Xuan, Y. Li, X. Xu, Z. Pan, Y. Li, Y. Luo, L. Sun, Three-dimensional printable magnetic hydrogels with adjustable stiffness and adhesion for magnetic actuation and magnetic hyperthermia applications, Gels 11 (2025) 67.
[46] M. Chen, G. Gong, L. Zhou, F. Zhang, Facile fabrication of a magnetic self-healing poly (vinyl alcohol) composite hydrogel, RSC Adv. 7 (2017) 21476–21483.
[47] B. Thapa, D. Diaz-Diestra, J. Beltran-Huarac, B.R. Weiner, G. Morell, Enhanced MRI T 2 Relaxivity in contrast-probed anchor-free PEGylated Iron oxide nanoparticles, Nanoscale Res. Lett. 12 (2017), https://doi.org/10.1186/s11671-017-2084-y.
[48] E.M. Nsengiyumva, P. Alexandridis, Xanthan gum in aqueous solutions: fundamentals and applications, Int. J. Biol. Macromol. (2022), https://doi.org/10.1016/j.ijbiomac.2022.06.189.
[49] S. Faria, C.L. De Oliveira Petkowicz, S.A.L. De Morais, M.G.H. Terrones, M.M. De Resende, F.P. De Frana, V.L. Cardoso, Characterization of xanthan gum produced from sugar cane broth, Carbohydr. Polym. (2011), https://doi.org/10.1016/j.carbpol.2011.04.063.
[50] V. Bhat, H.R. Shivakumar, R.K. Sheshappa, G. Sanjeev, Preparation and study on miscibility, thermal behavior of biocompatible polymer blends of xanthan gum-polyacrylamide, Int. J. Plast. Technol. (2014), https://doi.org/10.1007/s12588-014-9078-8.
[51] A. Srivastava, V. Mishra, P. Singh, A. Srivastava, R. Kumar, Comparative study of thermal degradation behavior of graft copolymers of polysaccharides and vinyl monomers, J. Therm. Anal. Calorim. (2012) 211–223, https://doi.org/10.1007/s10973-011-1921-y.
[52] M. Shah, A. Ullah, K. Azher, A. Ur Rehman, N. Akturk, W. Juan, C.S. Tüfekci, M. U. Salamci, The influence of nanoparticle dispersions on mechanical and thermal properties of polymer nanocomposites using SLA 3D printing, Crystals 13 (2023), https://doi.org/10.3390/cryst13020285.
[53] L.T.L. Nguyen, T.T. Nguyen, K.D. Nguyen, N.T.S. Phan, Metal-organic framework MOF-199 as an efficient heterogeneous catalyst for the aza-Michael reaction, Appl. Catal. A Gen. 425–426 (2012) 44–52, https://doi.org/10.1016/j.apcata.2012.02.045.
[54] N. Al-Janabi, P. Hill, L. Torrente-Murciano, A. Garforth, P. Gorgojo, F. Siperstein, X. Fan, Mapping the Cu-BTC metal-organic framework (HKUST-1) stability envelope in the presence of water vapour for CO2 adsorption from flue gases, Chem. Eng. J. 281 (2015) 669–677, https://doi.org/10.1016/j.cej.2015.07.020.
[55] L. Zhou, Z. Niu, X. Jin, L. Tang, L. Zhu, Effect of lithium doping on the structures and CO2 adsorption properties of metal-organic frameworks HKUST-1, ChemistrySelect 3 (2018) 12865–12870, https://doi.org/10.1002/slct.201803164.
[56] V. Gargiulo, A. Policicchio, L. Lisi, M. Alfe, CO2 capture and gas storage capacities enhancement of HKUST-1 by hybridization with functionalized graphene-like materials, Energy Fuel (2023), https://doi.org/10.1021/acs.energyfuels.2c04289.
[57] K.S. Walton, R.Q. Snurr, Applicability of the BET method for determining surface areas of microporous metal-organic frameworks, J. Am. Chem. Soc. 129 (2007) 8552–8556, https://doi.org/10.1021/ja071174k.
[58] N. Shaheed, S. Javanshir, M. Esmkhani, M.G. Dekamin, M.R. Naimi-Jamal, Synthesis of nanocellulose aerogels and Cu-BTC/nanocellulose aerogel composites for adsorption of organic dyes and heavy metal ions, Sci. Rep. (2021), https://doi.org/10.1038/s41598-021-97861-9.
[59] A. Garai, W. Shepherd, J. Huo, D. Bradshaw, Biomineral-inspired growth of metal-organic frameworks in gelatin hydrogel matrices, J. Mater. Chem. B (2013), https://doi.org/10.1039/c3tb20814a.
[60] J.Y.C. Lim, L. Goh, K.I. Otake, S.S. Goh, X.J. Loh, S. Kitagawa, Biomedically-relevant metal organic framework-hydrogel composites, Biomater. Sci. 11 (2023) 2661–2677, https://doi.org/10.1039/d2bm01906j.
[61] X. Dong, M. Fan, L. Zhao, K. Wang, Z. Hu, X. Liu, Recent advances in MOFs based hydrogels: from interactions, synthesis, and functionalization to food applications, Trends Food Sci. Technol. 166 (2025) 105415.
[62] A. Benny, S.D. Kalathiparambil Rajendra Pai, D. Pinheiro, S.J. Chundattu, Metal organic frameworks in biomedicine: innovations in drug delivery, Results Chem. (2024), https://doi.org/10.1016/j.rechem.2024.101414.
[63] W. Zou, L. Zhang, J. Lu, D. Sun, Recent development of metal–organic frameworks in wound healing: current status and applications, Chem. Eng. J. 480 (2024) 148220, https://doi.org/10.1016/j.cej.2023.148220.
[64] B.A. Sevinç, L. Hanley, Antibacterial activity of dental composites containing zinc oxide nanoparticles, J. Biomed. Mater. Res. 94 (2010) 22–31, https://doi.org/10.1002/jbm.b.31620.
[65] M. Tian, L. Zhou, C. Fan, L. Wang, X. Lin, Y. Wen, L. Su, H. Dong, Bimetal-organic framework/GOx-based hydrogel dressings with antibacterial and inflammatory modulation for wound healing, Acta Biomater. 158 (2023) 252–265, https://doi.org/10.1016/j.actbio.2022.12.049.
[66] M. Fandzloch, W. Bodylska, J. Trzcińska-Wencel, P. Golińska, K. Roszek, J. Wiśniewska, M. Bartmański, A. Lewińska, A. Jaromin, Cu-HKUST-1 and hydroxyapatite-the interface of two worlds toward the design of functional materials dedicated to bone tissue regeneration, ACS Biomater. Sci. Eng. (2023), https://doi.org/10.1021/acsbiomaterials.3c00594.
[67] S. Elmehrath, K. Ahsan, N. Munawar, A. Alzamly, H.L. Nguyen, Y. Greish, Antibacterial efficacy of copper-based metal-organic frameworks against *Escherichia coli* and *Lactobacillus*, RSC Adv. 14 (2024) 15821–15831, https://doi.org/10.1039/d4ra01241k.
[68] J. Xiao, S. Chen, J. Yi, H.F. Zhang, G.A. Ameer, A cooperative copper metal–organic framework-hydrogel system improves wound healing in diabetes, Adv. Funct. Mater. 27 (2017), https://doi.org/10.1002/adfm.201604872.
[69] S. Zhang, J. Ye, Z. Liu, H. Lu, S. Shi, Y. Qi, G. Ning, Superior antibacterial activity of Fe_3O_4@copper(ii) metal-organic framework core-shell magnetic microspheres, Dalton Trans. (2020), https://doi.org/10.1039/d0dt02417a.
[70] J. Li, Y. Yan, Y. Chen, Q. Fang, M.I. Hussain, L.N. Wang, Flexible curcumin-loaded Zn-MOF hydrogel for long-term drug release and antibacterial activities, Int. J. Mol. Sci. (2023), https://doi.org/10.3390/ijms241411439.
[71] F. Parsa, M. Setoodehkhah, S.M. Atyabi, Design, fabrication and characterization of a magnetite-chitosan coated iron-based metal–organic framework (Fe_3O_4@chitosan/MIL-100 (Fe)) for efficient curcumin delivery as a magnetic nanocarrier, RSC Adv. 15 (2025) 18518–18534.
[72] C. Tamames-Tabar, E. Imbuluzqueta, N. Guillou, C. Serre, S.R. Miller, E. Elkaïm, P. Horcajada, M.J. Blanco-Prieto, A Zn azelate MOF: combining antibacterial effect, CrystEngComm 17 (2015) 456–462, https://doi.org/10.1039/c4ce00885e.
[73] Z. Karimzadeh, S. Javanbakht, H. Namazi, Carboxymethylcellulose/MOF-5/graphene oxide bio-nanocomposite as antibacterial drug nanocarrier agent, BioImpacts 9 (2019) 5–13, https://doi.org/10.15171/bi.2019.02.
[74] N. Bhardwaj, S.K. Pandey, J. Mehta, S.K. Bhardwaj, K.H. Kim, A. Deep, Bioactive nano-metal-organic frameworks as antimicrobials against Gram-positive and Gram-negative bacteria, Toxicol. Res. (Camb). 7 (2018) 931–941, https://doi.org/10.1039/c8tx00087e.
[75] V. Coger, N. Million, C. Rehbock, B. Sures, M. Nachev, S. Barcikowski, N. Wistuba, S. Strauß, P.M. Vogt, Tissue concentrations of zinc, iron, copper, and magnesium during the phases of full thickness wound healing in a rodent model, Biol. Trace Elem. Res. 191 (2019) 167–176.